Materials Today Advances 28 (2025) 100661

Contents lists available at ScienceDirect

Materials Today Advances

journal homepage: www.journals.elsevier.com/materials-today-advances/

Biomimetic composite meta-stabilisers with programmable multi-directional quasi-zero stiffness and vibration isolation

Shawn Ravanbod [a], Kaveh Rahmani [a], Callum Branfoot [b], Sarah Karmel [c], Abdul Haque [d], Mark Lidgett [e], Arash M. Shahidi [f], Andrew Alderson [g], Mahdi Bodaghi [a,*]

[a] Department of Engineering, School of Science and Technology, Nottingham Trent University, Nottingham, NG11 8NS, UK
[b] Engineering Operations, National Composites Centre, Bristol, BS16 7FS, UK
[c] Rheon Labs, London, SW8 3QJ, UK
[d] Advanced Manufacturing Research Centre, Rotherham, S60 5TZ, UK
[e] Far-UK Ltd., Nottingham, NG11 7EP, UK
[f] Nottingham School of Art and Design, Nottingham Trent University, Nottingham, NG7 4HF, UK
[g] School of Engineering and Built Environment, Sheffield Hallam University, Sheffield, S1 1WB, UK

ARTICLE INFO

Keywords:
Mechanical metamaterials
Quasi-zero-stiffness
TPU/PHA
Woodpecker
Vibration isolation

ABSTRACT

This study introduces the first multidirectional quasi-zero-stiffness (QZS) meta-stabilisers that integrate bio-inspired curvilinear architectures with a sustainable polymer composite developed in this work. The QZS behaviour emerges synergistically from both structural design and nonlinear visco-hyper-elasticity of the newly developed bio-composite. Inspired by the woodpecker's tongue mechanism, the design leverages the interaction of geometry and material features to achieve exceptional damping and vibration isolation performance. The meta-stabilisers employ a Thermoplastic Polyurethane (TPU)/Polyhydroxyalkanoate (PHA) matrix reinforced with 2.5 wt% eggshell powder. It provides a bio-composite with 20 % higher tensile strength and 60 % greater energy dissipation than the unreinforced matrix. A hybrid computational framework, combining finite element modelling of nonlinear visco-hyper-elastic materials and AI-driven optimisation, enables precise control of the plateau region and constant-force output. The bio-composite generates a broad, stable plateau within 0.2–0.8 strain, perfectly matching the deformation regime of QZS structures. Experimental and numerical findings confirm stable QZS behaviour in three orthogonal directions, high vibration isolation capacity, repeatable hysteresis loops, and minimal Mullins effect over multiple cycles. In addition, the meta-stabilisers are programmable, where constant-force is tuneable between 0.5 and 220 N and displacement range between 1 and 7 mm. Under both periodic and random excitation, the meta-stabilisers achieved up to 100 % suppression of periodic vibrations and 77 % reduction under random vibrational off-road conditions. These results establish a new class of bio-inspired, sustainable, and programmable vibration control systems, offering a scalable, low-cost alternative to conventional active/passive noise/vibration/harshness solutions.

1. Introduction

Breaking through the limitations of conventional materials in terms of mechanical properties has long been a pursuit for researchers. As a solution, metamaterials exhibit exceptional mechanical properties that depend on their engineered patterns at macro and micro scales. These metamaterials can display a variety of mechanical characteristics, including enhanced tuneable stiffness [1], impact resistance [2], vibration absorption/dissipation [3,4], a negative Poisson's ratio [5], dual-target vibration mitigation and energy harvesting [6], shape morphing [7,8], and quasi-zero stiffness (QZS) [9]. To effectively control vibration propagation using conventional materials with low refractive indices, structures must be sufficiently thick or heavy, which renders them impractical. Recently, one of the most actively researched applications of metamaterials is in vibration isolation within low frequency ranges. Among the different types of Mechanical Metamaterials (MMs), QZS metamaterials have shown notable potential in vibration isolation and energy dissipation through their unique QZS mechanism. In a QZS system, the overall stiffness is engineered to be very close to zero over a specific range of displacements. This design allows the

* Corresponding author.
E-mail address: mahdi.bodaghi@ntu.ac.uk (M. Bodaghi).

https://doi.org/10.1016/j.mtadv.2025.100661
Received 25 September 2025; Received in revised form 21 October 2025; Accepted 9 November 2025
Available online 14 November 2025
2590-0498/© 2025 The Authors. Published by Elsevier Ltd. This is an open access article under the CC BY license (http://creativecommons.org/licenses/by/4.0/).

structure to deform significantly under applied forces while offering minimal resistance, thereby facilitating effective vibration isolation.

Many studies have explored the development of QZS structures using a variety of techniques such as inducing buckling in struts [10,11], incorporating oblique springs [12,13], or combining elements with both negative and positive stiffness [14–19]. In parallel, other meta-structure designs with QZS characteristics have been realised through scissor-like mechanisms [20–23], origami-inspired structures [24–26], shell-based systems [27–29], curvilinear beams [30–32], and bio-inspired architectures [33–36]. A common approach among these studies involves integrating positive and negative stiffness elements to achieve the QZS effect [37,38]. For instance, Chai et al. [39] introduced a linear stiffness compensation mechanism that combines positive and negative stiffness elements. This mechanism expands the QZS region, enhances load capacity, and provides excellent vibration isolation while maintaining stable equilibrium. However, this method often leads to larger or bulky structures and fabrication complexity, resulting in isolators that are not sufficiently compact for small-scale or space-constrained applications. Furthermore, many of these QZS meta-attenuators suffer from a limited operational displacement range. To address these limitations, recent research has focused on curvilinear, single-beam designs that enable the realisation of QZS behaviour within a compact, monolithic structure, referred to as monolithic QZS meta-structures.

Among the various QZS configurations, curved beam designs have attracted considerable attention due to their superior mechanical performance, including broader QZS displacement range, robustness to structural deviations, ease of fabrication, lightweight characteristics, and reliable load-bearing capacity. These features make curved and arc-shaped meta-structures especially suitable for applications requiring consistent force responses across extended displacement ranges. To name a few works; Zhang et al. [40] developed a curvilinear QZS meta-structure by optimising geometrical parameters using a genetic algorithm (GA). Ravanbod et al. [41] proposed an AI-assisted, bio--inspired curvy QZS meta-composite modelled on coral branches, which achieved programmable constant-force behaviour and an extended plateau region by varying both structural and material properties. They were the first to investigate the effect of curvilinear thickness variation tuned through a multi-objective genetic algorithm (multi-GA). Liu et al. [42] presented a 3D-printed wavy QZS metamaterial using photosensitive resin, which produced a constant force of approximately 2 N over a QZS region of about 3 mm. Liu et al. [43] designed a QZS device using four piezoelectric buckled beams and a vertical spring. This structure isolates vibrations and harvests energy by converting some vibrational energy into electricity while reducing energy transfer to the receiver. Zhao et al. [44] introduced a novel monolithic curved-beam QZS meta-structure that effectively reduced transmitted forces and enhanced vibration attenuation. Similarly, Liu et al. [45] proposed a unit cell inspired by the natural curvature of tree trunks, incorporating a curved beam structure optimised via GA to enhance QZS properties and vibration isolation performance.

Despite recent advances, significant challenges have remained. Most existing QZS metamaterials still suffer from large unit cell sizes, narrow plateau regions, and limited directional performance, typically restricted to a single axis. Crucially, the lack of multidirectional QZS isolators presents a major limitation, as such systems can only operate effectively in a fixed direction. To date, no comprehensive study has addressed the development of QZS isolators capable of functioning across multiple directions.

Moreover, although QZS metamaterials are required to support external loads (commonly referred to as payloads), most previous research has predominantly concentrated on optimising geometric configurations to enhance the QZS displacement range, thereby, overlooking the potential benefits of multi-material and multi-functional approaches. While the distinctive QZS behaviour is indeed largely attributed to structural geometry, material properties may also considerably influence key performance metrics such as constant-force output and energy absorption capacity. In particular, visco-hyper-elastic materials exhibiting hysteresis behaviour may offer substantial energy dissipation capabilities, owing to their intrinsic viscosity and pronounced elasticity. These materials can accommodate large deformations, thereby enabling greater energy damping during mechanical loading [46–49]. From this perspective, an avenue for advancing QZS structures involves not only geometric optimisation but also strategic material selection to tailor the constant-force (i.e., payload) level and enhance mechanical performance. For example, Ravanbod et al. [41] explored the role of hyper-elastic materials in improving the QZS behaviour and energy dissipation of meta-structures and demonstrated how material choice could be effectively employed as a design parameter for controlling force levels.

Motivated by the absence of a multidirectional, material-inclusive QZS system, this study presents the first programmable multidirectional QZS metamaterial, wherein both material and mechanical parameters contribute to the constant-force and plateau characteristics. Drawing inspiration from the structural and material configuration of the woodpecker's tongue, a novel curvilinear meta-structure was systematically developed, using an evolutionary multi-objective optimisation. The meta-stabilisers were fabricated using high-precision additive manufacturing and subsequently evaluated through numerical simulations and controlled experimental testing. Both monotonic and cyclic loading tests, conducted along three orthogonal directions, validated the multidirectional QZS behaviour and demonstrated the capacity for controllable mechanical properties. Additionally, the vibration transmission reduction performance of the proposed meta-stabilisers was quantified under configurations with and without the reinforced bio-composite. To demonstrate practical applicability, the meta-stabiliser was integrated into a remote-controlled (RC) vehicle to stabilise an onboard camera during motion. Real-case vibration attenuation tests confirmed its effectiveness in mitigating transmission across a range of operational conditions. The proposed multidirectional QZS meta-stabilisers are promising candidates for vibration control applications in the automotive sector, aerospace structures, and other engineering domains requiring lightweight yet multidirectional adaptive vibration isolators.

2. Conceptual design and modelling

This study aims to fundamentally explore the QZS behaviours of curvy beams in three dimensions, ranging from simple sine curves to multi-degree polynomials. It serves as a foundation for designing the next generation of curvilinear structures. A large array of wavy and helix beams can be established through a finite set of polynomial points. These polynomial structures are discretised via interpolation nodes, expressed in Cartesian coordinates $\{x, y, z\}$. The interpolation nodes delineate the structural mesh and define the polynomial geometry. Fig. 1 (a) illustrates the design space, highlighting the number of nodes and the boundary domains for the control parameters, along with their specified ranges of variation. In addition, various initial curvilinear beams were analysed, focusing on their force-displacement characteristics across the x-, y-, and z-directions under directional compression loading. The surface area of the beam is defined as a circle with a diameter of 2.5 mm, and the impact of varying the length along the curved beam (l) was also considered. Fig. 1(b) demonstrates that multiple wavy beams can be created, exhibiting different QZS behaviours while maintaining consistent length and weight. One notable advantage of curvy beams, as shown in Fig. 1, is that their multi-shaped and wavy configurations allow each section to function as a multi-stiffness mechanism. Consequently, the overall system's stiffness can be adjusted to be nearly zero, eliminating the necessity for combining a positive stiffness element with a negative stiffness element. Furthermore, the extensive design freedom available for curvy beams of constant length makes the optimisation process essential to ensure the structure achieves the widest plateau region in all directions.

The idea of a curvy beam with QZS characteristics for the proposed vibration isolator was inspired by the structure of a woodpecker's

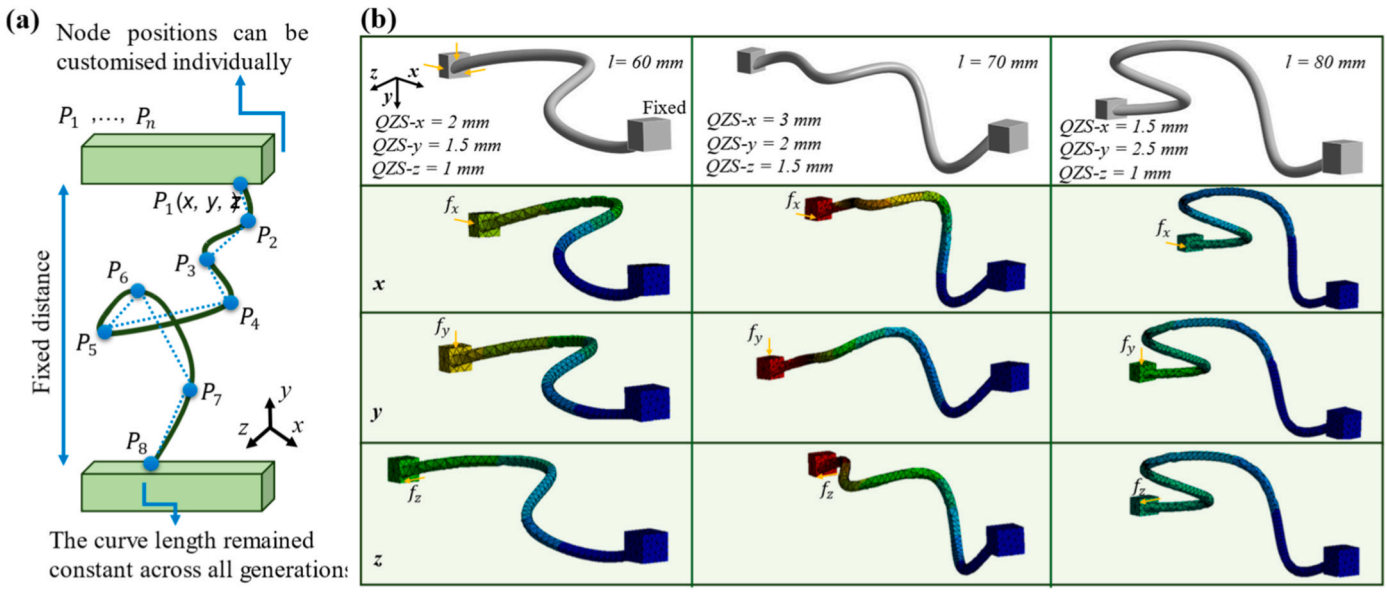


Fig. 1. Fundamental study of arbitrary curvature beams. **(a)** definition of design space for arbitrary curvature beams. **(b)** comparison of arbitrary curvature configurations with different lengths.

tongue. Literature indicates that the woodpecker's tongue wraps around its head, forming dual-curvy beams that shield its brain and skull from the impact and vibration forces experienced during drilling with its beak. When the bird pecks, the unique design of its tongue assists to dissipate these forces, thereby reducing strain on the brain. Zhu et al. [50] conducted a numerical study on the impact response of the woodpecker's head, finding that stress waves propagate from the upper bill to the back of the skull. They concluded that two features help reduce these stress waves: 1) the skull is wrapped with the hyoid apparatus (the tongue's structural mechanism), and 2) the viscoelastic energy absorption of the biological tissues (the material properties). In addition, Jung et al. [51] explained that the unusual shape of the hyoid apparatus and its unique mechanical properties contribute to energy dissipation and vibration isolation from both macro and micro structural perspectives. In addition to the structural aspects, studies have demonstrated that the material of the woodpecker's tongue possesses hyper-elastic properties, enabling high vibration absorption and energy dissipation. Zhou et al. [52] reported that the woodpecker's tongue exhibits remarkable strength and flexibility due to its specialised composite microstructure. This tongue consists of a flexible cartilage and bone skeleton covered by a thin layer of highly elastic tissue. The stress-strain behaviour of the woodpecker's tongue was examined through tensile tests, which revealed its hyper-elastic and high-strength characteristics. Wang et al. [53] provided a detailed analysis of the biomechanics involved, noting how the tongue's elasticity and tissue arrangement facilitate energy absorption in a manner similar to

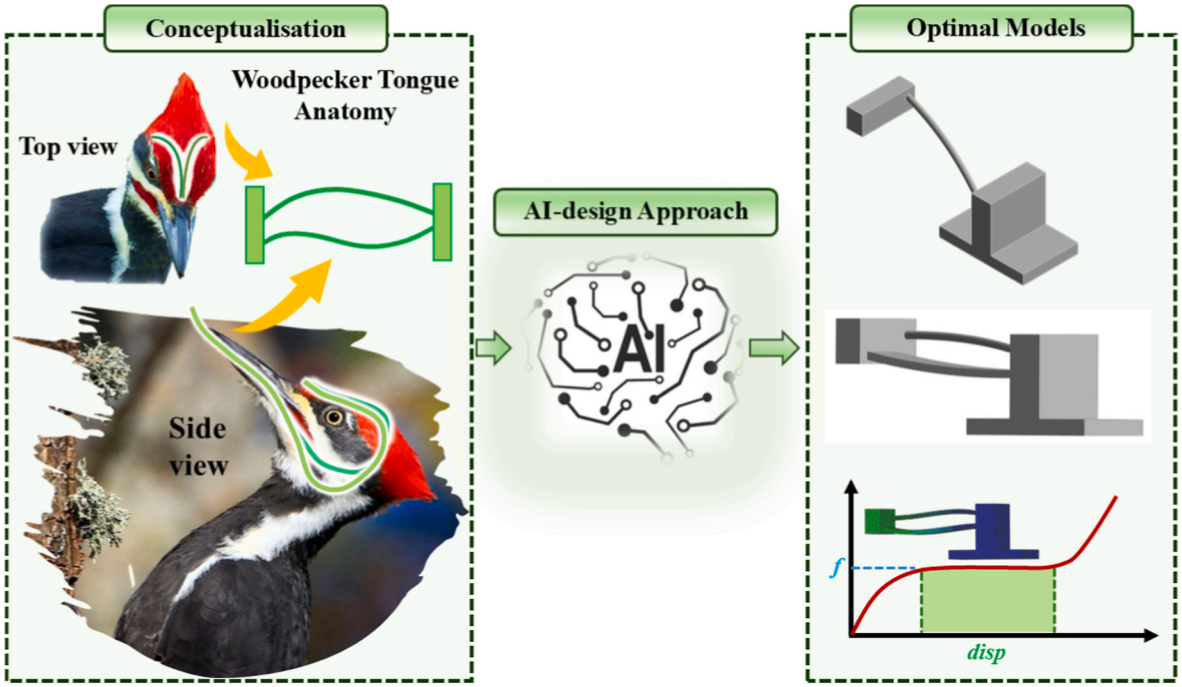


Fig. 2. Topological design process from inspiration to final structure.

engineered structures.

Consequently, both the structural design and material characteristics of the woodpecker's tongue have inspired this study to develop hyperelastic curvy beam isolators with QZS properties. Fig. 2 schematically illustrates the design evolution of curvy beam meta-oscillators. As demonstrated, the shape of the woodpecker's tongue resembles a Y-shape. The half of the tongue was initially modelled as a single unit-cell and subsequently developed a supercell by arranging two unit-cells to create a complete representation of the tongue. Two biomimetic QZS meta-oscillators were designed using an AI-assisted method, which will be discussed further in this section. Model I features a single wavy beam capable of generating QZS characteristics in all directions. To enhance payload capacity, Model II was developed with two curves that mimic the whole tongue shape, allowing it to withstand higher force levels.

A multi-GA was employed to automatically generate an optimal design using a novel evolutionary design methodology, beginning from an initial model. Five control parameters were defined to shape the polynomial curve. Each point's location governed by its coordinates in the x, y, and z directional components as depicted in Fig. 3. These control points were introduced within a 3D domain to investigate whether the 3D geometry of the mechanical metamaterial could influence its QZS properties. Unlike previous studies predominantly focused on 2D QZS structures fabricated in the xy-plane, this work explores a truly 3D configuration to address a gap in the current literature. These structural parameters serve as design variables in the optimisation process, guiding the multi-GA towards configurations that yield the optimum mechanical response. The bounds for each parameter are detailed in Table 1 and schematically explained in Fig. 3. The optimisation objective was to simultaneously maximise the plateau region in both the x- and y-directions, represented by the objective functions $\varnothing_1$ and $\varnothing_2$, respectively. The objective functions and constant-force criteria are defined in Fig. 4 and are formulated as follows:

$$\varnothing_1 = \max\,(d_{x_i}),\ \text{where } f_{x_{end}} - f_{x_{start}} = d_{x_i}, i = 0:1:N$$

$$(i)\begin{cases} For\ j = 1:1:100 \\ If\ \dfrac{f_{x_{j+1}} - f_{x_j}}{f_{x_j}} \le 10\% \rightarrow f_{x_j} = f_{x_{start}} \\ For\ j = start:1:100 \\ If\ \dfrac{f_{x_j} - f_{x_{start}}}{f_{x_{start}}} > 10\% \rightarrow f_{x_j} = f_{x_{end}} \end{cases} = \gg QZS_x = f_{x_{end}} - f_{x_{start}} = d_{x_i} \quad (1)$$

Table 1
Controlling points with their determined changing range.

Parameter	Range
P_1	P_x (0:10), P_y (-5:25), P_z (0:23),
P_2	P_x (11:15), P_y (-5:25), P_z (0:23),
P_3	P_x (16:30), P_y (-5:25), P_z (0:23),
P_4	P_x (31:40), P_y (-5:25), P_z (0:23),
P_5	P_x (41:46), P_y (-5:25), P_z (0:23),

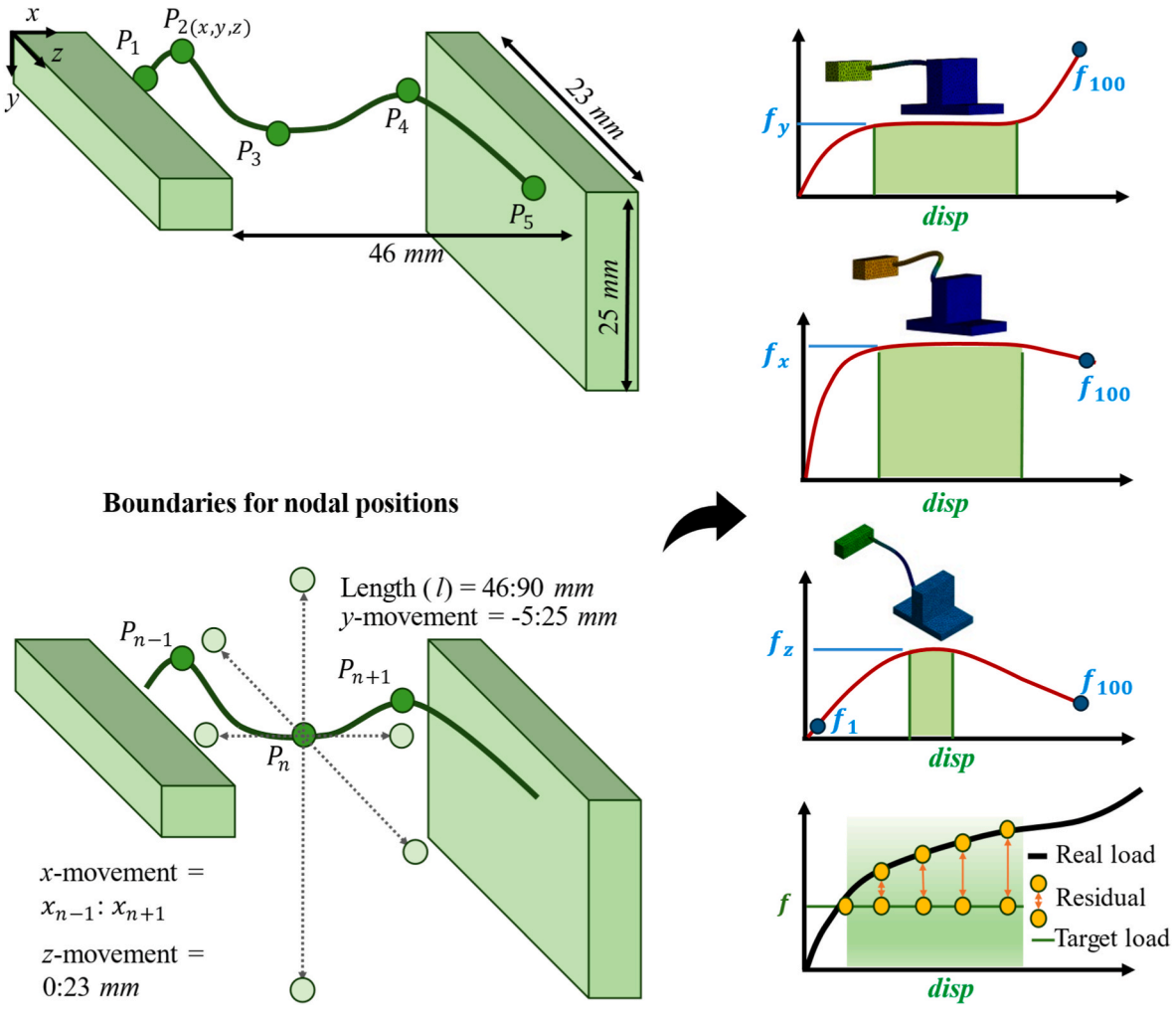


Fig. 3. Illustration of the search domain for individual control points during the AI-driven design process. This targeted search strategy enables localised refinement while maintaining global coherence, facilitating an adaptive design process.

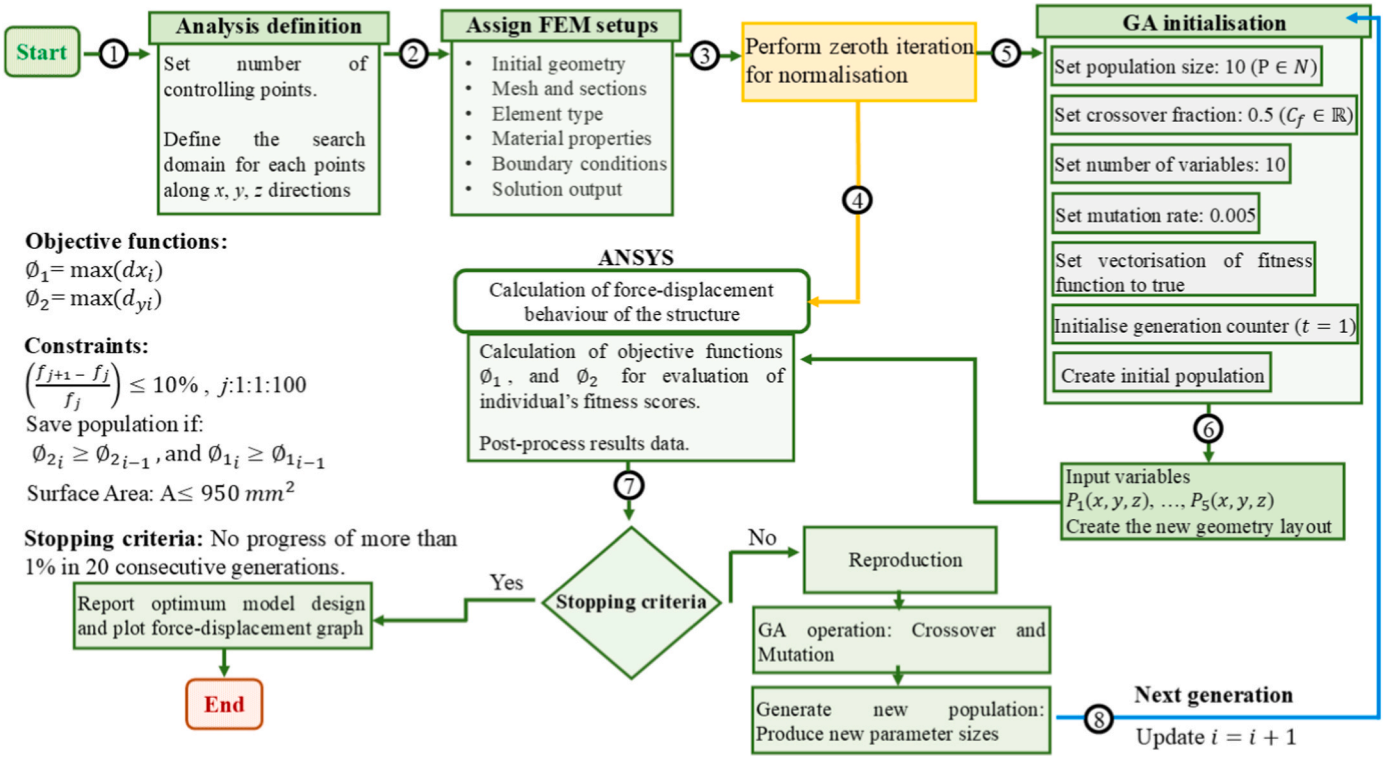


Fig. 4. Flowchart detailing the implementation of the multi-GA process through the integration of the MATLAB-ANSYS Livelink approach.

$$\varnothing_2 = \max\left(d_{y_i}\right), \text{where } f_{y_{end}} - f_{y_{start}} = d_{y_i}, i = 0:1:N$$

$$(i)\begin{cases} For\ j = 1:1:100 \\ If\ \dfrac{f_{y_{j+1}} - f_{y_j}}{f_{y_j}} \le 10\% \rightarrow f_{y_j} = f_{y_{start}} \\ For\ j = start:1:100 \\ If\ \dfrac{f_{y_j} - f_{y_{start}}}{f_{y_{start}}} > 10\% \rightarrow f_{y_j} = f_{y_{end}} \end{cases} = \gg QZS_y = f_{y_{end}} - f_{y_{start}} = d_{y_i} \quad (2)$$

In this analysis, force-displacement curves along the *x*-, *y*-, and *z*-directions are obtained from 100 data points saved in an Excel file (indexed by *j*), while *i* represents the number of iterations performed. Also, the criterion for determining the QZS state has been defined as $\left(f_{j+1} - f_j\right)/f_j \le 10\%$, meaning that the reaction force variation within the QZS region does not exceed 10 %.

To facilitate this process, FEM using ANSYS (Version 2024R1, Ansys Inc., Canonsburg, PA, USA) was integrated with MATLAB (Version R2023b, The MathWorks Inc., Natick, MA, USA). This coupling enables the algorithm to dynamically update control parameters based on performance feedback and subsequently provide new geometry configurations for evaluation via FEM analysis. As outlined in the flowchart (Fig. 4), this iterative loop begins with the multi-GA receiving simulation results from ANSYS, evaluating them against defined criteria, and generating new populations of parameter values for the next iteration. An iteration is retained as the basis for the next generation if the objective function values of the newly generated population exceed those of the previous iteration; the current population then serves as the parent for subsequent evolution. The updated geometries would be re-simulated, and the process will continue until convergence is achieved. The specifications of the optimisation process, including algorithm parameters and control settings, are provided in Table 2 and further illustrated in Fig. 4.

Ultimately, Fig. 5(a) reports the optimisation outcomes, where the multi-GA identified a novel 3D curved QZS mechanical metamaterial design, as shown in Fig. 5(b). The optimised structure exhibits a significantly enhanced plateau region, approximately 5 mm in the *x*-direction and 3.2 mm in the *y*-direction, while generating a 1.5 mm QZS length along *z*-direction as displayed in Fig. 6. This design represents a breakthrough in the field, as it is the first known 3D QZS structure capable of generating plateau regions in multiple directions.

3. Material development

This study presents a novel multifunctional metamaterial whose functionality arises not only from its structural behaviour but also from its material characteristics, including enhanced mechanical strength, hyper-elasticity, and effective energy dissipation. To this end, a hyper-elastic bio-composite was developed for the proposed QZS meta-stabilisers, in which its constituent material properties were inspired by the unique biomechanical properties of the woodpecker's tongue as explained in Fig. 7.

The host matrix of the bio-composite was prepared by a 50:50 wt% blend of Polyhydroxyalkanoate (PHA) and Thermoplastic Polyurethane (TPU). Other blend ratios, including 30(TPU):70(PHA) wt.%, 70(TPU):30 (PHA), 60(TPU):40(PHA), and 40(TPU):60(PHA) wt.%, were also tested. However, the 50:50 wt% composition provided the best balance between flexibility and stiffness. The present work used Nanovia TPU pellets with a Shore hardness of 93A and a melting temperature of 185 °C, and PHA pellets supplied by ColorFabb with a melting temperature of 190 °C. PHAs

Table 2
Specification of the proposed multi-GA procedure.

Multi-GA properties	Value
Algorithm	Multi-objective GA
Number of iterations used	287
Execution time for each iteration (Minutes)	80
Convergence time (Minutes)	21300
Algorithm's output	$\varnothing_1 = 3.2$ mm, $\varnothing_2 = 5$ mm

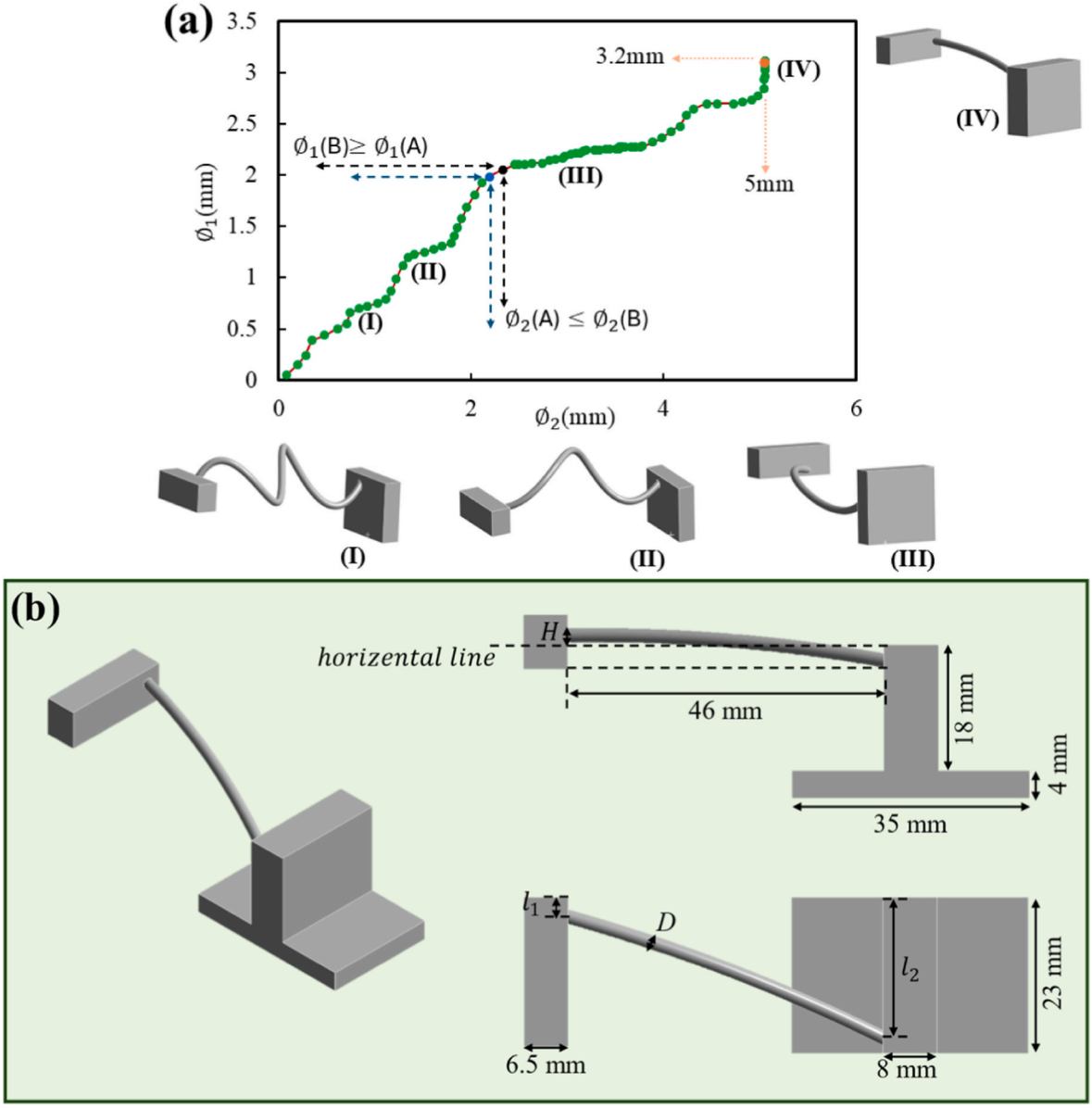


Fig. 5. AI-driven design outcomes. **(a)** Results from the algorithm showing that the objective functions achieved QZS regions of 5 mm and 3.2 mm in the *x*- and *y*-directions, respectively. **(b)** The optimised curvy beam geometry.

are a family of biodegradable and bio-based polyesters synthesised by various microorganisms, which serve as a sustainable alternative to traditional petroleum-derived polymers. These materials typically demonstrate elastic behaviour under small deformations. TPU, known for its high elasticity and softness, further contributes to the flexibility of the matrix. However, the resulting TPU/PHA blend is relatively soft and has a limited load-bearing capacity. Therefore, eggshell powder (EGS) sourced from Aniforte was incorporated as a reinforcement agent to enhance the mechanical performance of the composite. EGS has received attention as a low-cost and environmentally friendly material, particularly in biomedical [54] and energy storage applications [55] (e.g., lithium-ion and sodium-ion batteries), due to its high calcium content and inherently porous microstructure.

The uniform dispersion of particles is a critical aspect of composite development, which notably affects mechanical properties and printability. Experimental observations during filament fabrication revealed that EGS content above 7.5 wt% leads to increased brittleness and reduced interlayer adhesion. As a result, the maximum reinforcement was 7.5 wt%. Fig. 8 illustrates the key steps in the fabrication process of the EGS-reinforced TPU/PHA bio-composite filaments. These steps include the preparation of raw materials (TPU, PHA, and EGS), followed by planetary ball milling, filament extrusion, and 3D printing. Prior to processing, all materials were dried individually in a hot-air oven at 70 °C for 24 h to remove moisture. TPU and PHA pellets were first blended in equal weight proportions to form the base matrix. Subsequently, varying wt.% of EGS powder were incorporated into this matrix. The mixtures were subjected to planetary ball milling to ensure homogeneous dispersion of EGS particles within the polymer blend. The resulting mixtures were then dried again at 70 °C for 12 h prior to the extrusion process. A single-screw extruder (3devo, Netherlands) comprising 4 individually-controlled heat zones was utilised to produce filaments with a diameter of 1.75 mm. Extrusion parameters, including temperature profile and extrusion speed, were carefully optimised to minimise defects and ensure dimensional consistency of the filaments. Detailed extrusion conditions are provided in Table 3. It is worth noting that cross-sections of the extruded filaments were examined to determine if the EGS particles were homogeneously dispersed and to identify any agglomerates.

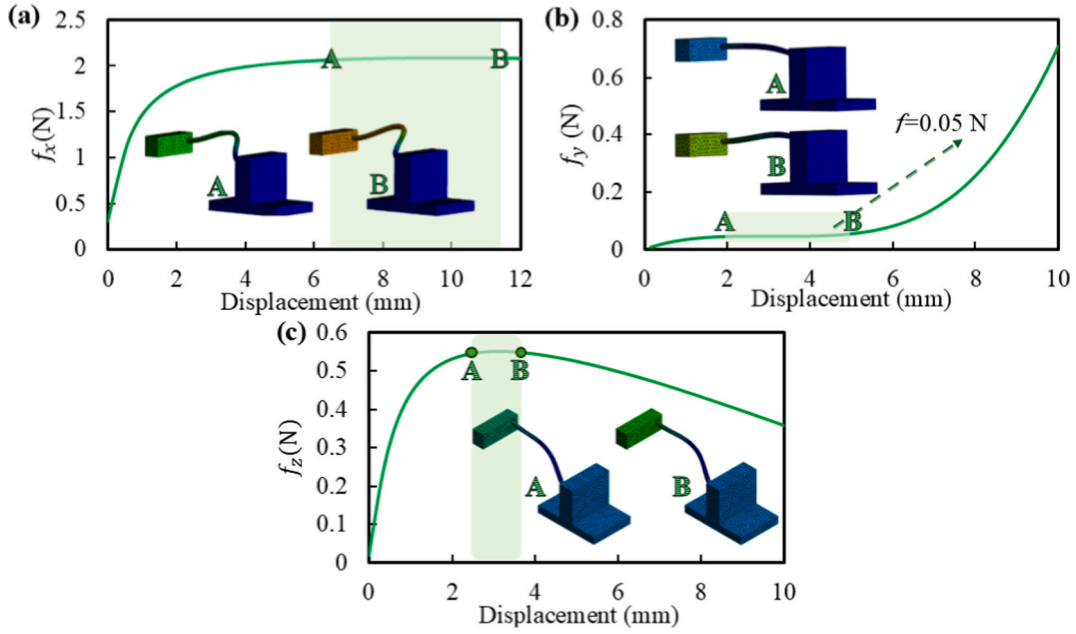


Fig. 6. Force-displacement response of the AI-driven Model I in three orthogonal directions. **(a)** illustrates the QZS region and corresponding force levels along the *x*-direction. **(b)** depicts the QZS region and force response in the *y*-direction. **(c)** presents the QZS behaviour and associated force characteristics in the *z*-direction.

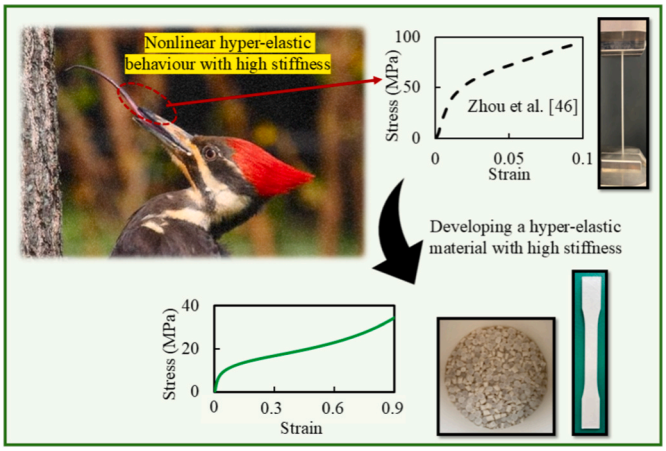


Fig. 7. Design inspirations underpinning the development of the proposed bio-composites.

To fabricate the samples, a Fused Filament Fabrication (FFF) 3D printing technique was employed. Both standard dog-bone tensile specimens and the proposed metamaterial structures were manufactured using a Bambu Lab X1C 3D Printer. The process parameters, including nozzle temperature, bed temperature, print speed, and layer height, were carefully optimised to ensure high print quality and consistent mechanical performance across all sample types. The complete set of 3D printing parameters used during the fabrication process is summarised in Table 4.

4. FEM simulations

ANSYS software was utilised to numerically calculate the mechanical features, employing the FEM as the primary solving tool. To calibrate the FEM prior to running metamaterial simulations, a dog-bone sample was 3D printed from a TPU/PHA blend with 2.5 % EGS, following the ASTM-D-638 Type-I standard, and subsequently tested experimentally at a speed of 5 mm/min. The experimental stress-strain data were then imported into ANSYS for analysis. A nonlinear hyper-elastic material

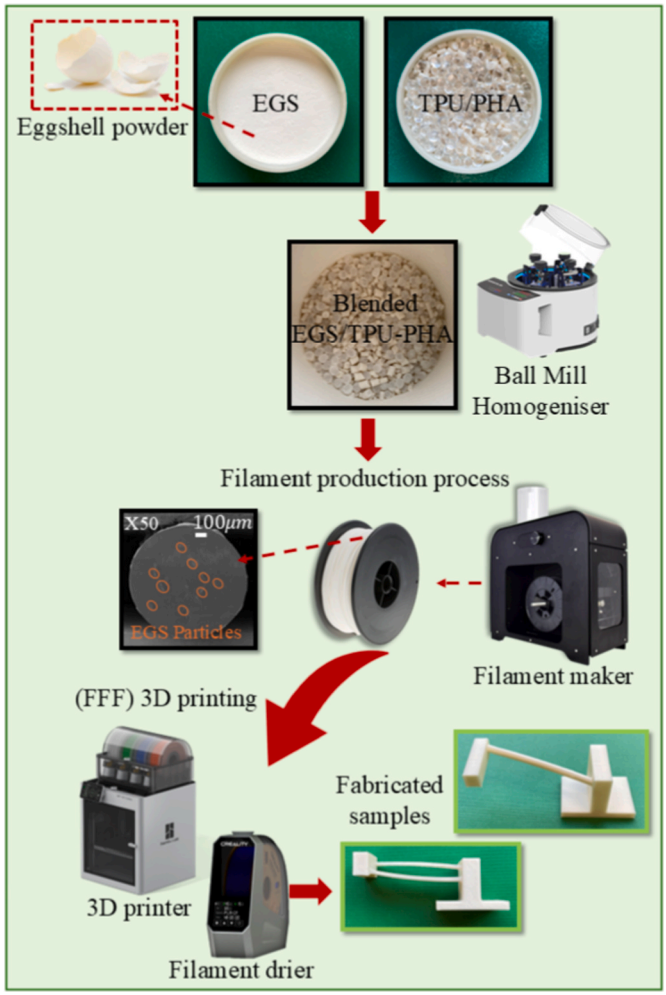


Fig. 8. Schematic illustration of the bio-composite production process.

Table 3
The extrusion factors used in producing bio-composite filaments.

Parameters	Value (TPU/PHA)	Value (%EGS/TPU-PHA)
Extrusion temperature at heat zone 1 (°C)	170	170
Extrusion temperature at heat zone 2 (°C)	185	190
Extrusion temperature at heat zone 3 (°C)	180	185
Extrusion temperature at heat zone 4 (°C)	170	170
Die temperature (°C)	180	185
Filament diameter (*mm*)	1.75	1.75
Extrusion speed (rpm)	3.5	3.5

Table 4
3D printing parameters used in the manufacturing process.

Parameters	Value
Nozzle temperature (°C)	200
Bed temperature (°C)	60
Infill density (%)	100
Nozzle diameter (*mm*)	0.4
Layer thickness (*mm*)	0.2
Printing speed (*mm/s*)	60

model was selected for the numerical analysis due to the hyper-elastic behaviour exhibited by the fabricated bio-composites (refer to Fig. 9). A comprehensive investigation was carried out to evaluate the accuracy of existing hyper-elastic solving models by comparing their results with experimental data. Ultimately, the hyper-elastic Mooney-Rivlin model with five parameters (H-MR5) was chosen for simulations under monotonic loading conditions. After this calibration, the dog-bone sample was simulated and subjected to monotonic loading that replicated the boundary conditions employed in the experimental tests. In accordance with the established boundary conditions, the force-displacement behaviour of the structures was examined under three distinct loading directions: *x*, *y*, and *z*. The base of the structure was fixed, replicating a cantilever beam configuration. For the *x*-direction study of the QZS system, an external force was applied at the tip of the beam along the *x*-axis, while movement in the *y*-and *z*-directions was constrained. The same methodology was employed for the analyses in the *y*-and *z*-directions, with the force applied correspondingly and displacements constrained in the other two directions. In the mesh study, the mesh refinement technique (MRT) was employed with a constant-force convergence of 1 %. The chosen mesh type was a hexahedral mesh with an element size of 0.1 mm.

Furthermore, the designed meta-stabilisers were examined numerically to assess their QZS behaviour, energy dissipation, and mode shapes under both monotonic and cyclic loading conditions. In the case of monotonic loading, the FEM analysis was performed within the structural static domain using the H-MR5 model. While, the cyclic analysis employed FEM simulation in the transient structural domain, employing a visco-hyper-elastic material model that integrated the Mooney-Rivlin five-parameter model with the Prony series (VH-MR5). The boundary conditions applied in these analyses were consistent with those used in the experimental setup.

5. Experimental analysis

This section outlines the methodologies and procedures employed in the conducted experiments. It provides a detailed description of the mechanical testing protocols under both static and dynamic loading conditions, along with the vibration testing procedures.

5.1. Mechanical test

The mechanical properties of the reinforced bio-composites were evaluated through uniaxial tensile tests using a Shimadzu AG-X Plus machine with a 1 kN load cell. For this purpose, dog-bone specimens were fabricated in accordance with ASTM D638 Type I standards for different composite formulations: TPU, PHA, TPU/PHA, 1.5 %, 2.5 %, 5 %, and 7.5 % EGS-reinforced TPU/PHA. Fig. 9 illustrates printed dog-bones along with their geometric dimensions.

Each composition was tested using five replicate samples to account for variability arising from the fabrication and 3D printing processes. The average values from these tests were used to report the mechanical properties. Tensile tests were carried out at a constant crosshead speed of 5 mm/min. Each specimen was placed between screw-action grips, with the upper grip applying the tensile load while the lower grip remained fixed. Residual strain was measured 24 h after testing to allow the material to return to its original position.

In addition, the proposed QZS meta-structures were subjected to both monotonic and cyclic compression tests to investigate their force-displacement response and energy dissipation characteristics. For monotonic compression along the *x*-direction, a displacement of 12 mm was applied to the lateral surface (*x*-side) of the structure. The meta-

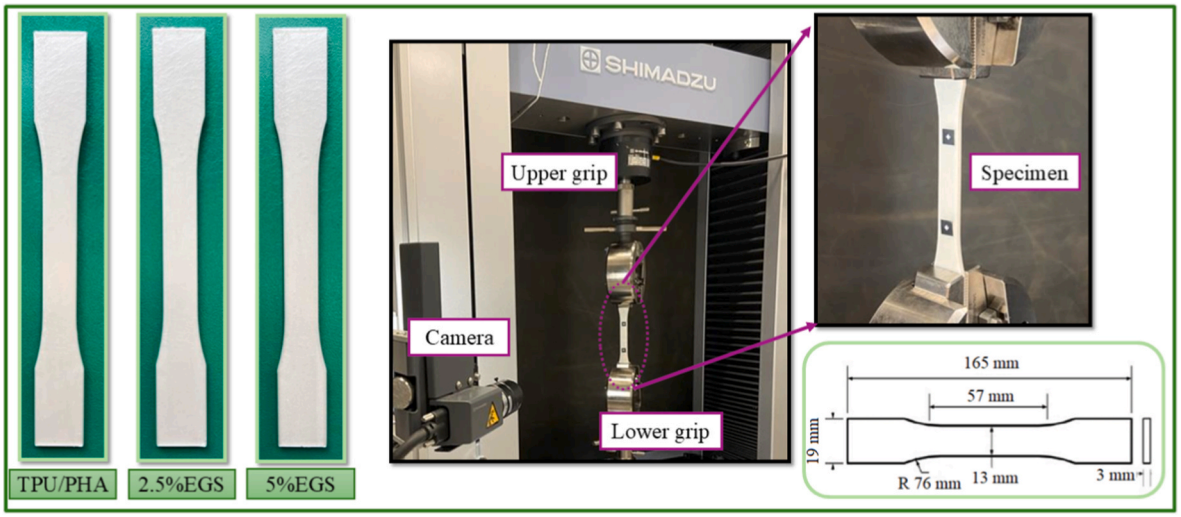


Fig. 9. 3D-printed dog-bone specimens made from reinforced bio-composites, shown alongside the tensile testing setup used to evaluate their mechanical properties.

structures were supported by a 3D-printed cage to constrain motion along the *y*- and *z*-axes, thereby simulating fixed boundary conditions (visit Figures (19-20)). The base of each sample was securely fastened to the lower grip of the Shimadzu testing machine. Compression was applied at a constant rate of 5 mm/min. The same setup was used for the cyclic compression tests, which included an unloading phase following the 12 mm compression. Compression testing along the *y*-direction/*z*-direction involved a similar setup, where a displacement of 10 mm was applied to the top surface (*y*-side/*z*-side).

5.2. Vibration test

This study evaluates the vibration isolation performance of QZS meta-stabilisers (Model I and Model II). The models were fabricated using TPU/PHA with and without 2.5 % reinforcement to elucidate the influence of material composition on vibration mitigation characteristics. To realistically simulate operational load-bearing conditions, additional weights equal to the constant-force were applied to the meta-stabilisers. The experimental setup comprised a shaker (TIRA VIB GmbH), capable of delivering a maximum thrust of 0–400 N over a frequency range of 2–20000 Hz, a power amplifier, a dynamic signal analyser, two wireless accelerometers, and a laptop computer for data acquisition as depicted in Fig. 10. The shaker was driven by an excitation signal, transmitted through the amplifier to induce vibration. One accelerometer was mounted on the specimen's top surface to measure transmitted acceleration, while the other was placed on the specimen's base to record the input excitation. Data collected over the relevant frequency spectrum were processed to generate vibration isolation spectra.

Considering the QZS characteristics depicted in Fig. 18, Model II with 2.5 % EGS-reinforced TPU/PHA exhibited a plateau zone at a constant force level of approximately 0.9 N along the *y*-direction and 36 N along the *x*-direction. Consequently, weights of 90 *g* and 3.6 kg (the accelerometer mass was included) were affixed to the upper end of the specimen along the *y*- and *x*-axes, respectively. Similarly, for the pure TPU/PHA counterpart, a constant-force region of approximately 0.73 N (corresponding to 70 *g* as determined in Fig. 17) along the *y*-axis test and 29.3 N (approximately 2.93 kg) along the x-axis test dictated the choice of applied weights to simulate the operational constant-force region. For Model I with 2.5 % EGS-reinforced TPU/PHA, which demonstrates a QZS at force levels of approximately 0.7 N along the y-direction, 24.1 N along the *x*-direction, 7.2 N along *z*-direction, weights of approximately 70 *g*, 2.41 kg, and 0.72 kg were applied to replicate the mechanical loading conditions along each axis. Fig. 10 illustrates the vibration test setup for Model I and Model II. Further, a parametric analysis was performed to explore the effects of varying excitation accelerations (g) and the frequency study on the vibration isolation performance and dynamic response of both models. These experiments aimed to assess the systems' robustness under different vibrational intensity levels. The detailed results and their implications are discussed comprehensively in the subsequent Results and Discussion section.

6. Results and discussion

This section commences by emphasising the improved material properties of the reinforced bio-composite in comparison to the individual base materials: TPU, PHA, and their TPU/PHA blend. Particular attention is given to key mechanical characteristics, including tensile strength under both monotonic and cyclic loading, as well as hysteresis energy dissipation. Furthermore, the mechanical performance of the designed QZS meta-stabilisers is investigated using different material configurations. Finally, vibration isolation capabilities of designed meta-stabilisers are evaluated across a range of excitation conditions and frequency domains.

6.1. Mechanical properties of bio-composites

The tensile strength and stress-strain behaviours of 3D-printed bio-composites made from TPU/PHA reinforced with EGS particles at weight percentages of 0 %, 1.5 %, 2.5 %, 5 %, and 7.5 % were evaluated according to ASTM D638-Type I standards, as shown in Fig. 11. To indicate that the uncertainties in the experimental values are within acceptable ranges, the standard deviation (SD) was reported for each set of averaged experimental data. The experimental tensile tests (Fig. 11 (II)) indicate that pure PHA exhibits a linear elastic behaviour, with a fracture point corresponding to a maximum stress of 19 MPa at 6 %

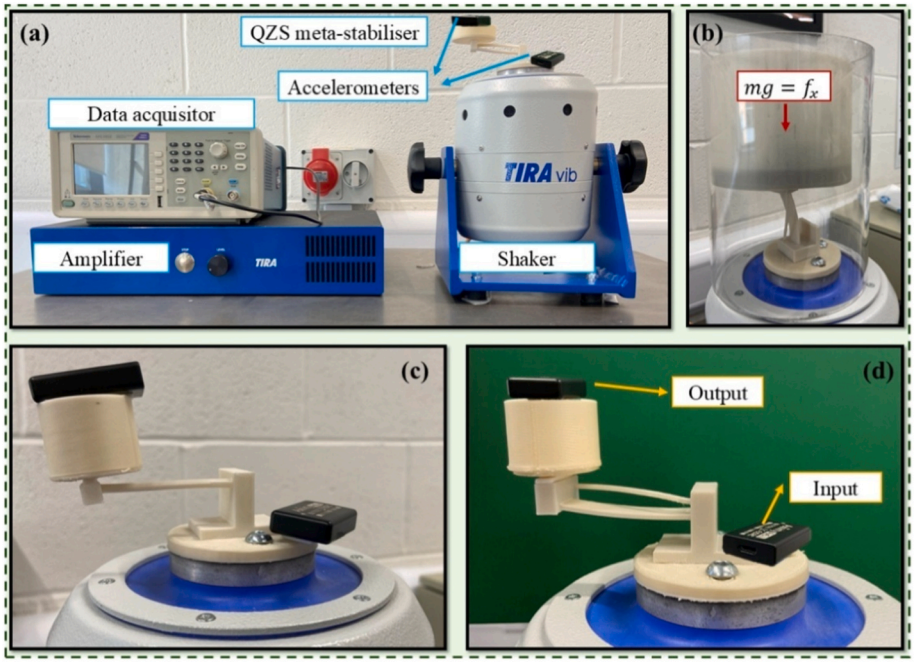


Fig. 10. Experimental vibration test setup of QZS metamaterials. **(a)** overview of the experimental setup. **(b)** vibration test of Model II under *x*-direction excitation. **(c)** and **(d)** vibration test of Model I and Model II under *y*-direction excitation, respectively.

strain. In contrast, TPU demonstrates a non-linear hyper-elastic performance characterised by significant deformability. However, it possesses low stiffness (4.8 MPa at 50 % strain), which limits its applicability in engineering scenarios that require high load-bearing capacity under substantial deformation. As a result, a TPU/PHA composite was fabricated that displayed acceptable hyper-elasticity and flexibility, coupled with medium stiffness. Notably, the incorporation of 2.5 % EGS particles into the TPU/PHA significantly improved the material's stiffness. However, the results presented in Figs. 11(I) and (II), and **11(IV)** demonstrate that the stiffness values decrease with both lower and higher additions beyond the 2.5 % EGS threshold. This may be due to: 1) reduced filament uniformity affecting print quality and density; and 2) particle agglomeration causing micro-voids that hinder stress transfer.

Fig. 11(I) illustrates the engineering stress-strain behaviour of composites. It is evident that the TPU/PHA composite interestedly features a relative plateau region spanning from 20 % to 50 % strain. Furthermore, the incorporation of EGS particles as reinforcement not only boosts the stiffness of the TPU/PHA composite but also flattens the plateau region, expanding it from 20 % to 80 % at higher strains, as highlighted in the magnified inset of Fig. 11(I). This composite is promising for

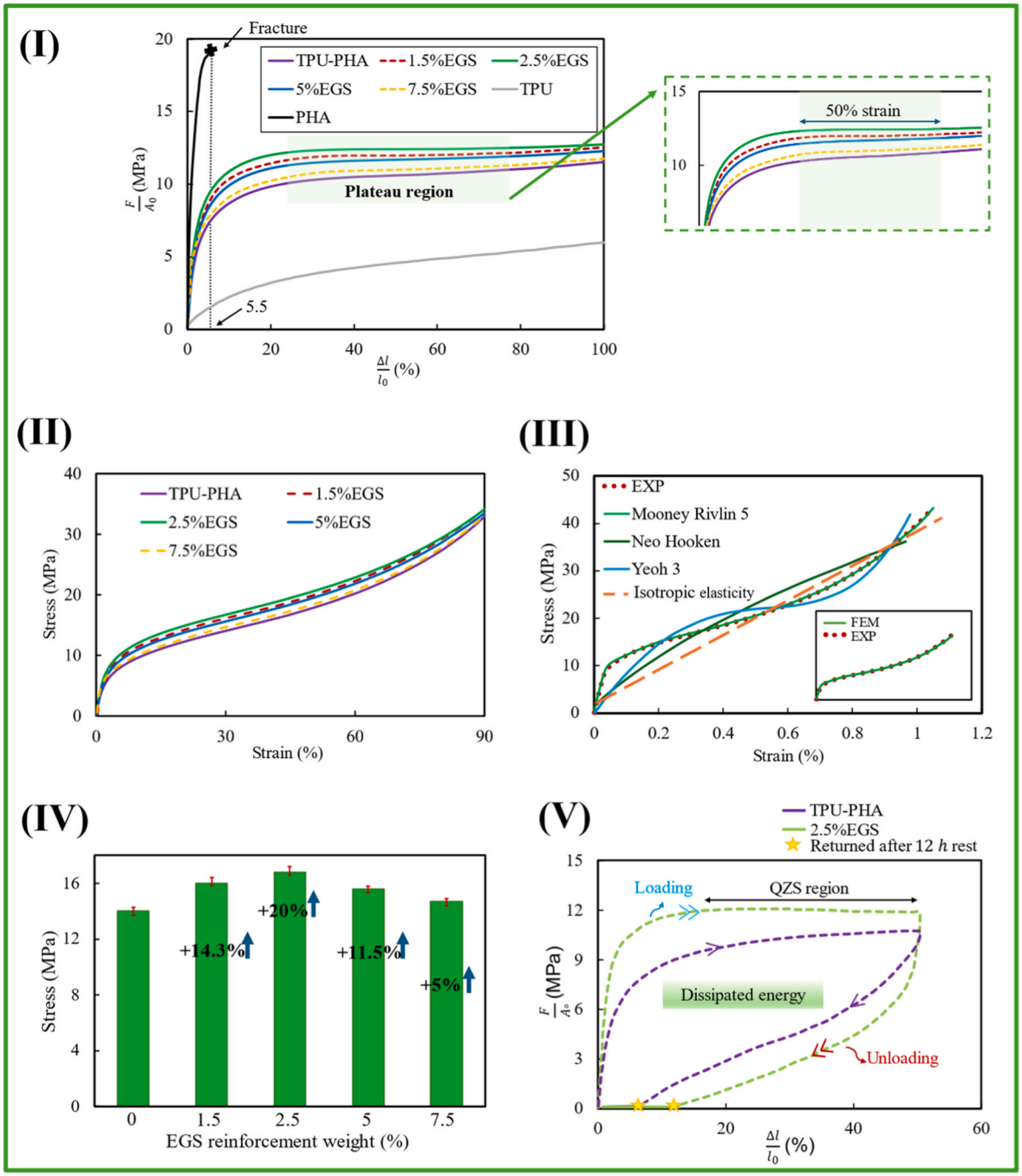


Fig. 11. Mechanical performance of the developed bio-composites. **(I)** comparison of the engineering stress-strain response of the 3D-printed composites and the base materials, illustrating that EGS powder reinforcement introduces an extended plateau region. **(II)** true stress-strain behaviour of the composites. **(III)** correlation between FEM simulations using the H-MR5 model and experimental results. **(IV)** stress values at 30 % strain for different reinforcement levels (The red gauge bar shows the deviation range in the experimental data). **(V)** cyclic tensile testing of the 2.5 % EGS-reinforced TPU/PHA composite up to 50 % strain, revealing no residual strain.

applications that require significant deformation and flexibility while maintaining a high load-bearing capacity. Additionally, the material possesses QZS properties, suggesting that its use in the manufacturing of QZS metamaterials could enhance their energy absorption and QZS characteristics from both material and geometric perspectives. This represents a novel finding, demonstrating that a material can generate a plateau region purely through its intrinsic properties rather than structural design. Furthermore, comparison of the QZS responses between TPU/PHA and 2.5 % EGS-reinforced TPU/PHA reveals that the addition of EGS reduces force-level fluctuations and yields a more stable, flatter plateau region. This phenomenon is being further explored in vibration isolation tests to evaluate the practical benefits of reinforcement in enhancing QZS stability and performance.

Fig. 11(III) confirms the validity of the proposed FEM based on the H-MR5 model, with less than 3 % deviation at large strain. This calibrated FEM is employed for simulating meta-bio-composites in later sections. Various linear and nonlinear material models were investigated, including Neo-Hookean, Yeoh (third-order), H-MR5, and linear isotropic elasticity. Comparison with experimental data revealed that the H-MR5 model provided satisfactory convergence and agreement with the observed results. Consequently, the H-MR5 model was adopted for monotonic compression analysis. For cyclic compression loading, the VH-MR5 model was employed to enhance simulation efficiency.

Fig. 11(IV) illustrates the stiffness of the developed bio-composites at 30 % strain. It is evident that a 2.5 % EGS reinforcement results in a 20 % increase in stiffness; however, this improvement diminishes when the percentage of reinforcement is reduced or increased. The red gauge bar indicates the data deviations observed during the experiments. Additionally, Fig. 11(V) investigates the cyclic loading behaviour of the 2.5 % EGS-reinforced TPU/PHA composite. The findings reveal that the bio-composite demonstrates visco-hyper-elastic characteristics during cyclic loading, with no residual strain observed. Moreover, the area under the stress-strain curve reflects the material's energy dissipation capabilities. It is observable that 2.5 % EGS reinforcement generates 4.52 $M\frac{J}{m^3}$. When compared to the TPU/PHA, the EGS reinforcement not only enhances overall stiffness by 22 % but also contributes to an extended plateau region with an increased energy dissipation of 60 %. One micromechanical mechanism that may contribute to the QZS with enhanced energy dissipation performance is the behaviour of material particles within hyper-elastic materials. These particles can be envisioned as interconnected networks of spring-like elements capable of absorbing energy and converting it into kinetic form. Owing to their exceptional deformability and elastic characteristics, such materials can experience substantial deformations and subsequently recover their original configuration, thereby enabling efficient storage and dissipation of mechanical energy.

Furthermore, Scanning Electron Microscopy (SEM) was employed to examine the microstructure of the composites, with particular attention to bonding quality, defects, agglomeration, printing accuracy, and overall uniformity. The observations were conducted using a JSM-7100F LV FEG microscope. To enhance image clarity, all samples were coated

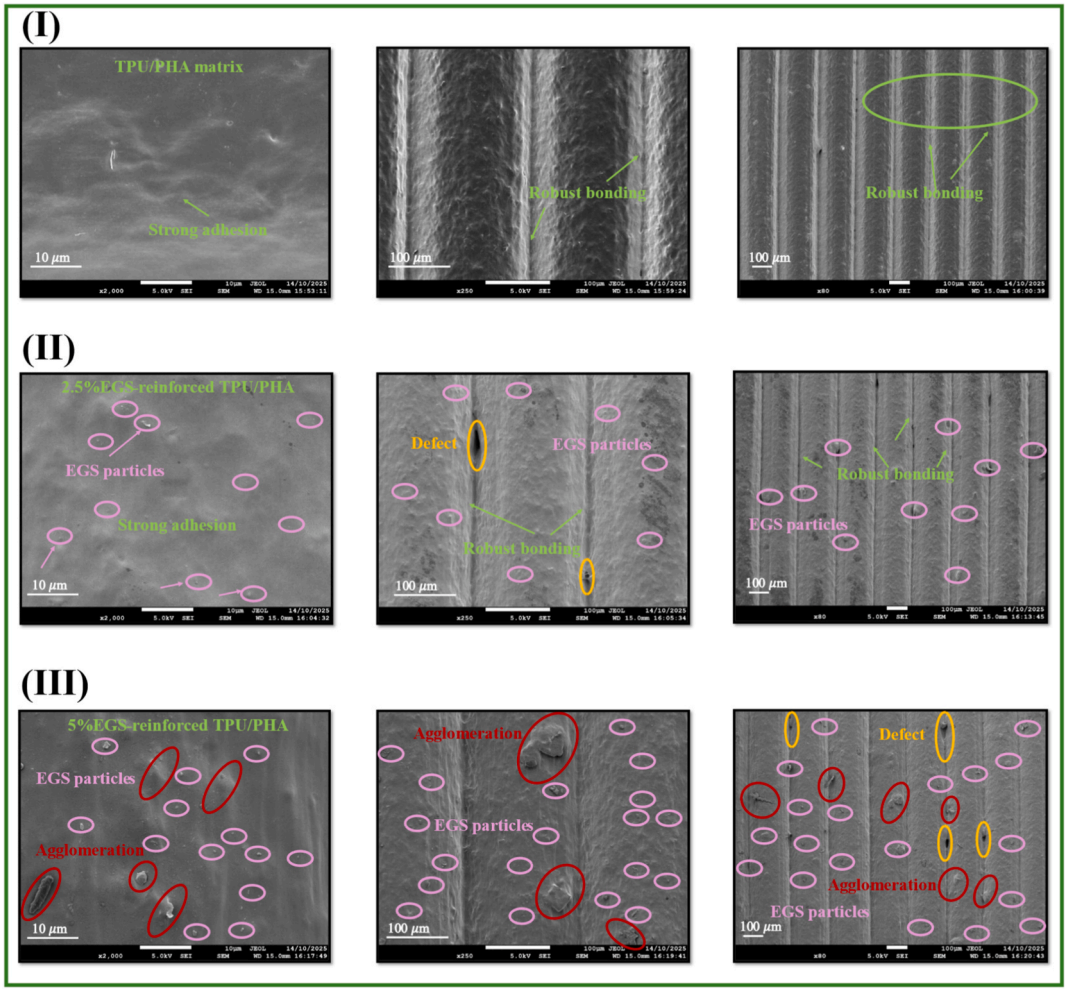


Fig. 12. SEM images of the printed bio-composites. **(I)** The microphotograph of the pure TPU/PHA composite. **(II)** The microphotograph of the 2.5 % EGS-reinforced TPU/PHA composite, showing improved interfacial adhesion and minimal voids. **(III)** The microphotograph of the2.5 % EGS-reinforced TPU/PHA composite, highlighting increased agglomeration and defects.

with a thin 10 nm layer of gold prior to imaging. As shown in Fig. 12(I), the SEM images of the printed TPU/PHA specimen reveal a uniform and well-bonded microstructure with minimal voids, suggesting effective impregnation and good wet-out of the matrix. Fig. 12(II) further highlights strong interlayer contact in the 2.5 wt% EGS-reinforced TPU/PHA composite, again with few voids, confirming efficient bonding between layers. The enhanced interfacial adhesion observed in both the pure TPU/PHA and the 2.5 wt% EGS-reinforced composite indicates a well-integrated structure. During tensile testing, localised matrix deformation and damage were evident due to the applied stress. However, the EGS particles distributed along the interfaces appeared to inhibit the propagation of layer breakage, thereby enhancing the composite's resistance to failure. This behaviour likely explains the increased strength observed with the inclusion of EGS particles. Additionally, the improved energy dissipation capability can be attributed to both chemical and mechanical interlocking between the TPU/PHA matrix and the EGS particles. The introduction of EGS creates multiple micro-interfaces within the composite, where frictional slippage occurs under external loading. This mechanism effectively dissipates mechanical energy, contributing to the improved damping performance of the bio-composite. Conversely, at higher EGS contents (5 wt%), the composite shows a noticeable increase in agglomeration and defect formation, as illustrated in Fig. 12(III). These defects compromise the interfacial bonding and surface quality of the printed material. Consequently, during tensile loading, cracks and layer separation tend to initiate and propagate from these regions, leading to reduced mechanical performance. Therefore, EGS reinforcement levels above 2.5 wt% appear to deteriorate both the mechanical properties and the printing quality of the TPU/PHA composite.

6.2. Mechanical properties of QZS meta-stabilisers

This section outlines the mechanical characteristics and QZS features of two proposed multidirectional QZS meta-stabilisers, namely Model I

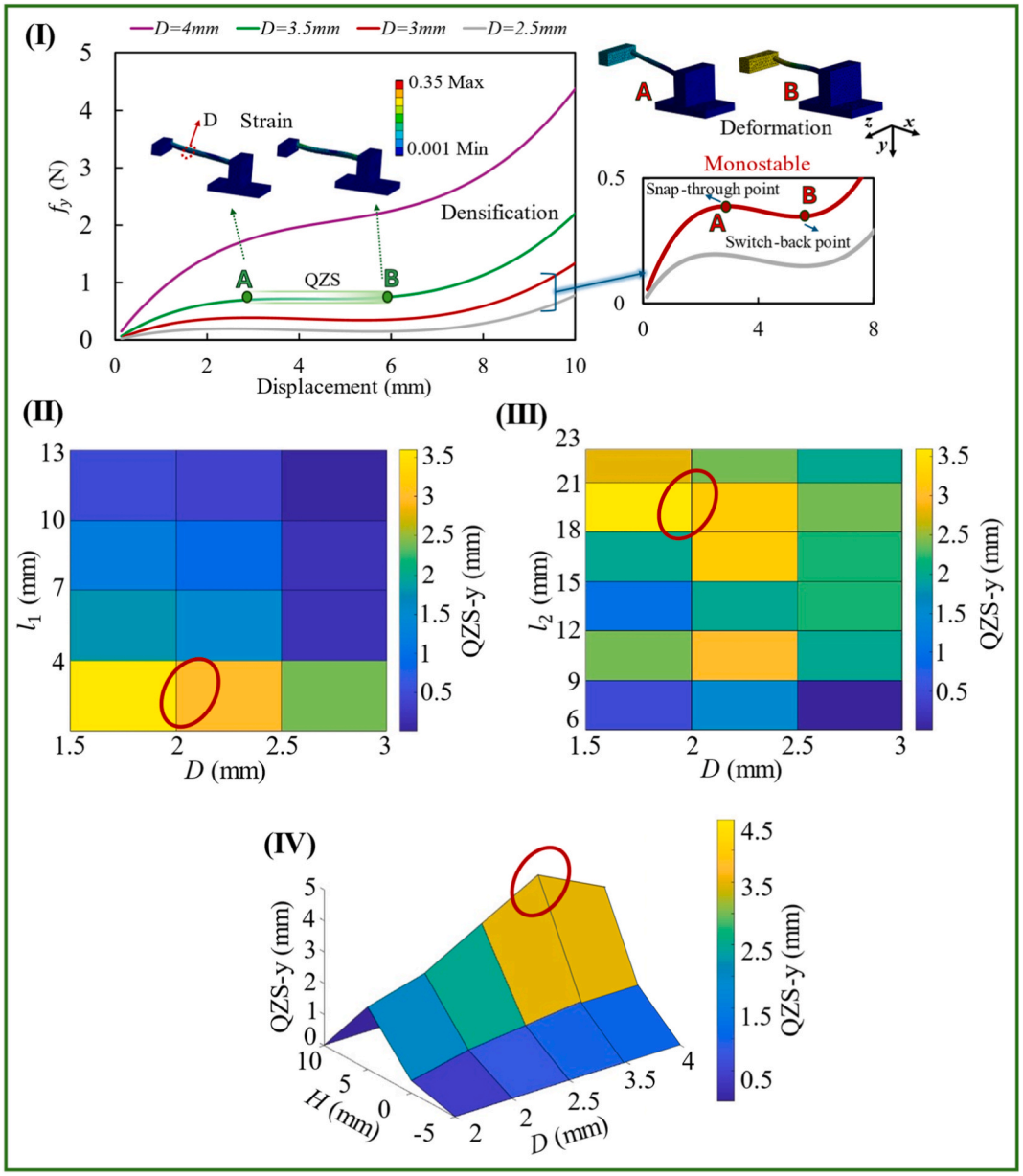


Fig. 13. Influence of structural features on the QZS properties along the *y*-direction. **(I)** variation in reaction force and QZS length as a function of D, while $l_1 = 1$ mm, $l_2 = 21$ mm, and $H = 5$ mm. **(II)** QZS length variation with respect to changes in l_1 and D, while $l_2 = 21$ mm, and $H = 5$ mm **(III)** QZS length variation with respect to l_2 and D while $l_1 = 1$ mm, and $H = 5$ mm. **(IV)** QZS length variation as a function of H and D, while $l_1 = 1$ mm, and $l_2 = 21$ mm.

and Model II along three-directions. The materials used for both experimental and numerical investigations are TPU/PHA as the base material, and 2.5 % EGS-reinforced TPU/PHA as the reinforced composite with their material properties determined in earlier sections. In the initial stage, the impact of structural factors on mechanical properties is depicted in Figures (13-15), stemming from an extensive parametric study. To perform the sensitivity analysis, the value of the studied parameter is varied while the other parameters are kept at their optimal values. This analysis allows us to specify the most effective geometric parameters before implementing the optimisation analysis, thereby reducing the number of structural parameters considered during the optimisation process.

Fig. 13(I) illustrates the variation in the FEM calculated QZS length and constant-force level as a function of the circular cross-section of curved the beam(D) along y-direction. It is observed that the reaction force level increases with increasing D. For $D = 2.5$ mm and $D = 3$ mm, a snap-through phenomenon is evident, which can contribute to energy dissipation. Notably, at $D = 3.5$ mm, a wider QZS region of approximately 3.2 mm is formed, maintaining a nearly constant force of 0.7 N. Fig. 13(II) and 13(III) demonstrate the influence of varying horizontal (l_1) and vertical (l_2) segment lengths, respectively, in relation to different D values on QZS characteristics. The results indicate that $l_1 = 1$ mm and $l_2 = 21$ mm can lead to an extended QZS region. Fig. 13(IV) presents the effect of the distance between the beam ending section and the horizontal line (H) shown in Fig. 5(b) on QZS behaviour. The maximum QZS region is achieved at $H = 5$ mm and $D = 3.5$ mm, beyond which the QZS length begins to decline. According to the force-displacement characteristics along z-direction, Fig. 14(I) shows that increasing l_2 raises the force level and shifts the transition point from positive to negative stiffness. Fig. 14(II) illustrates the development of QZS behaviour as a function of l_1. Specifically, $l_1 = 1$ mm produces a distinct QZS region with a transition point labelled as point A, which is accompanied by the corresponding mode shape. Fig. 14(III) reveals that increasing D results in a higher force level and shifts the QZS region toward a larger displacement range. Fig. 14(IV) presents the force-displacement response as a function of H, where $H = 5$ mm produces a QZS region approximately 1.5 mm in length. Considering x-direction, Fig. 15(I) investigates the QZS characteristics as a function of D. A substantial QZS region of 5 mm at a force level near 2 N is observed for $D = 2$ mm. Fig. 15(II) and 15(III) evaluate the impact of l_1 and l_2 variations, respectively, under different D values. The configurations with $l_1 = 1$ mm and $l_2 = 21$ mm consistently yield longer QZS regions than other combinations. Finally, Fig. 15(IV) explores the influence of H on QZS properties. It is found that $H = 5$ mm enhances the QZS length up to 5 mm.

Model II was developed to regulate force levels, while preserving QZS characteristics. This model biomimetically replicates the complete structural geometry of a woodpecker's tongue by employing a dual-curvilinear configuration, as illustrated in Fig. 2. Various geometrical profiles were investigated for the surface area of the second curvature, referred to as the *supportive curve*. Fig. 16 presents Model II incorporating different surface shapes for this supportive curve, including circular, elliptical, rectangular, and straight-slot configurations. The surface area of the supportive curve was maintained constant at $A = 6.3\ mm^2$ in all cases. As shown in Fig. 16(I), the circular and rectangular configurations produce QZS regions of approximately 3 mm and 3.3 mm with a nearly constant force around 0.5 N along the y-direction, respectively. Fig. 16(II) demonstrates that the rectangular surface yields an extended QZS zone of approximately 5 mm, with a nearly constant force of 10 N along the x-direction. Moreover, Fig. 16(III) reveals that the circular configuration generates a bi-stable QZS region approximately 1 mm in length along the z-direction.

Based on these findings, the rectangular surface was selected for the supportive curve in Model II. A subsequent parametric analysis was conducted to optimise its geometric dimensions. The finalised

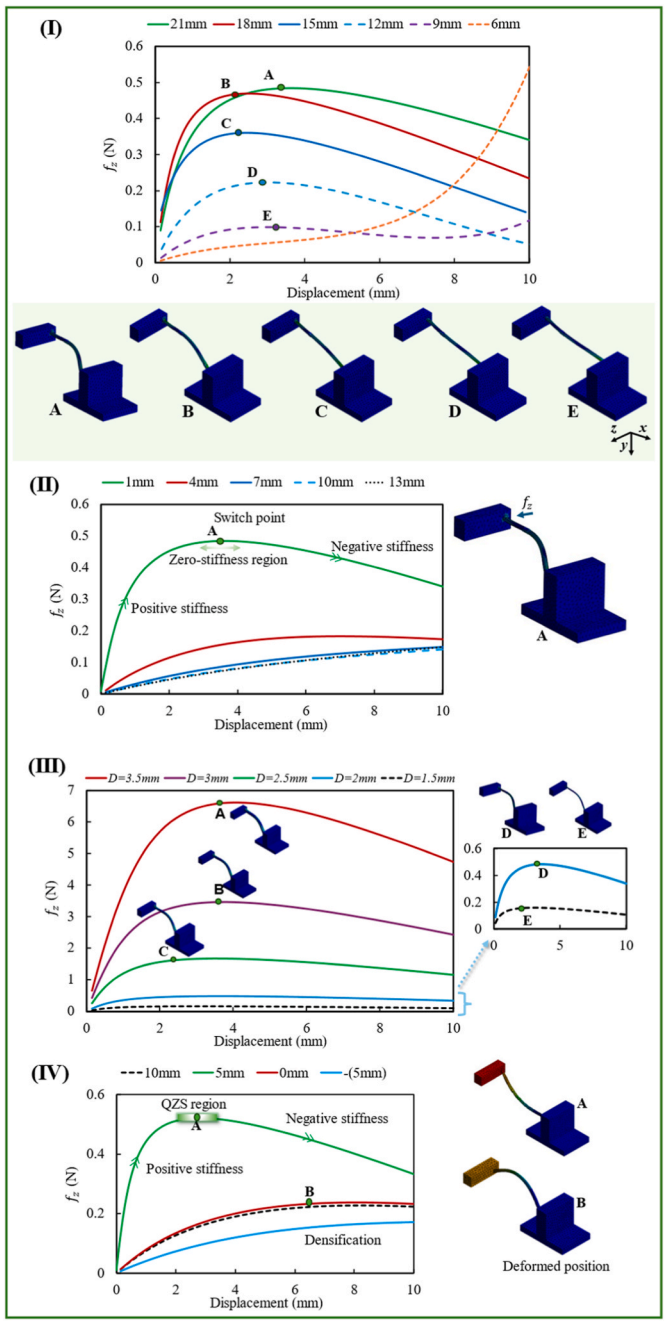


Fig. 14. Influence of structural features on the QZS properties along the z-direction. **(I)** variation in reaction force and displacement as a function of l_2, while $l_1 = 1$ mm, $D = 2$ mm, and $H = 5$ mm. **(II)** force-displacement variation with respect to changes in l_1, while $l_2 = 21$ mm, $D = 2$ mm, and $H = 5$ mm **(III)** force-displacement variation with respect to D, while $l_1 = 1$ mm, $l_2 = 21$ mm, and $H = 5$ mm. **(IV)** QZS properties variation as a function of H, while $l_1 = 1$ mm, $l_2 = 21$ mm, and $D = 2$ mm.

configuration of Model II is depicted in Fig. 17(I). In addition, the effects of the rectangular cross-section dimensions, specifically width (W) and length (L), on both the QZS region and the constant force level are examined in Fig. 17(II) and 17(III). Results indicate that increasing the length L enhances the force level with minimal adverse effect on the QZS length. Conversely, increasing the width W leads to a reduction in the QZS region while improving the force output. This highlights a necessary trade-off between the desired force magnitude and the QZS region length. Ultimately, the dimensions $L = 12.5$ mm and $W = 1.75$ mm were selected as optimal values, as they yielded a stable and high-level

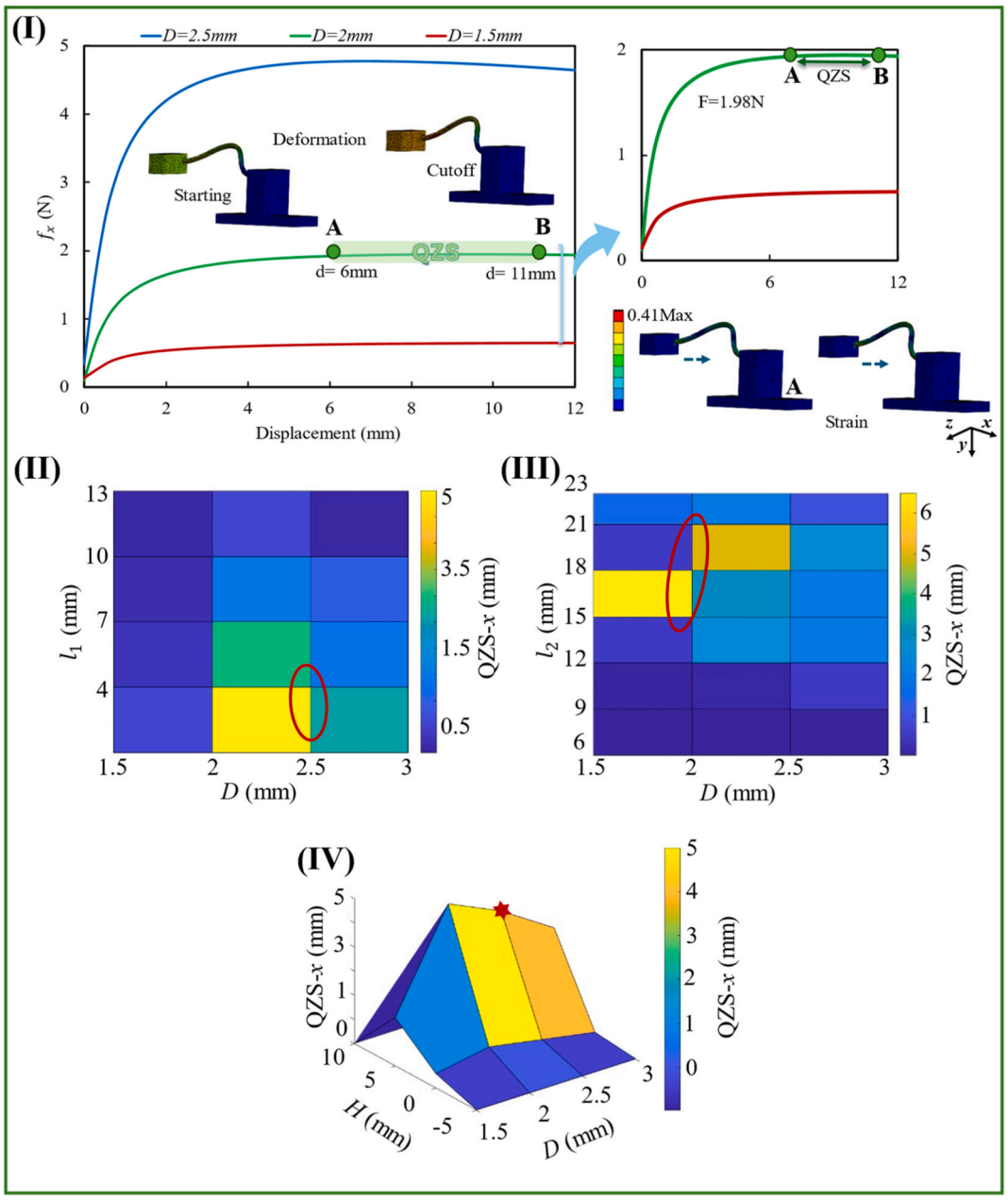


Fig. 15. Influence of structural features on the QZS properties along the *x*-direction. **(I)** variation in reaction force and QZS length as a function of *D*, while $l_1 = 1$ mm, $l_2 = 21$ mm, and $H = 5$ mm. **(II)** QZS length variation with respect to changes in l_1 and *D*, while $l_2 = 21$ mm, and $H = 5$ mm **(III)** QZS length variation with respect to l_2 and *D*, while $l_1 = 1$ mm, and $H = 5$ mm. **(IV)** QZS length variation as a function of *H* and *D*, while $l_1 = 1$ mm, and $l_2 = 21$ mm.

constant force. The finalised meta-stabiliser is capable of programmable behaviour, producing constant force outputs ranging from 0.1 N to 2 N and QZS regions from 0.5 mm to 3.5 mm under *y*-directional excitation. Under *x*-directional excitation, it can deliver constant force levels from 5 N to 40 N and QZS regions spanning 1 mm–6.5 mm, all within a single unit cell. This design enables broad tuneability, allowing users to precisely set the desired force level, the initiation point and length of the plateau zone.

6.3. Experimental results of mechanical tests

Experimental and FEM analyses were conducted under varying monotonic and cyclic loading conditions in order to examine the mechanical performance of curved QZS meta-stabilisers. Two material systems were studied: TPU/PHA and 2.5 % EGS-reinforced TPU/PHA composites. To minimise the impact of manufacturing and printing variability on mechanical characteristics, five meta-samples of each composite were fabricated and tested. The reported mechanical responses reflect the average results obtained from these five specimens.

Furthermore, to compute the dissipated energy and total energy absorption of the metamaterials, the relationship between these energy metrics and the force-displacement response of the mechanical system can be established. The total energy absorbed during deformation is defined as the area under the loading portion of the force-displacement curve, which reflects the work done by external forces on the structure as follows.

$$EA = \int_0^{\delta_{max}} F_{load}(\delta)d\delta \tag{3}$$

where *EA* is the energy absorbed (Joules), F_{load} is the applied force as a

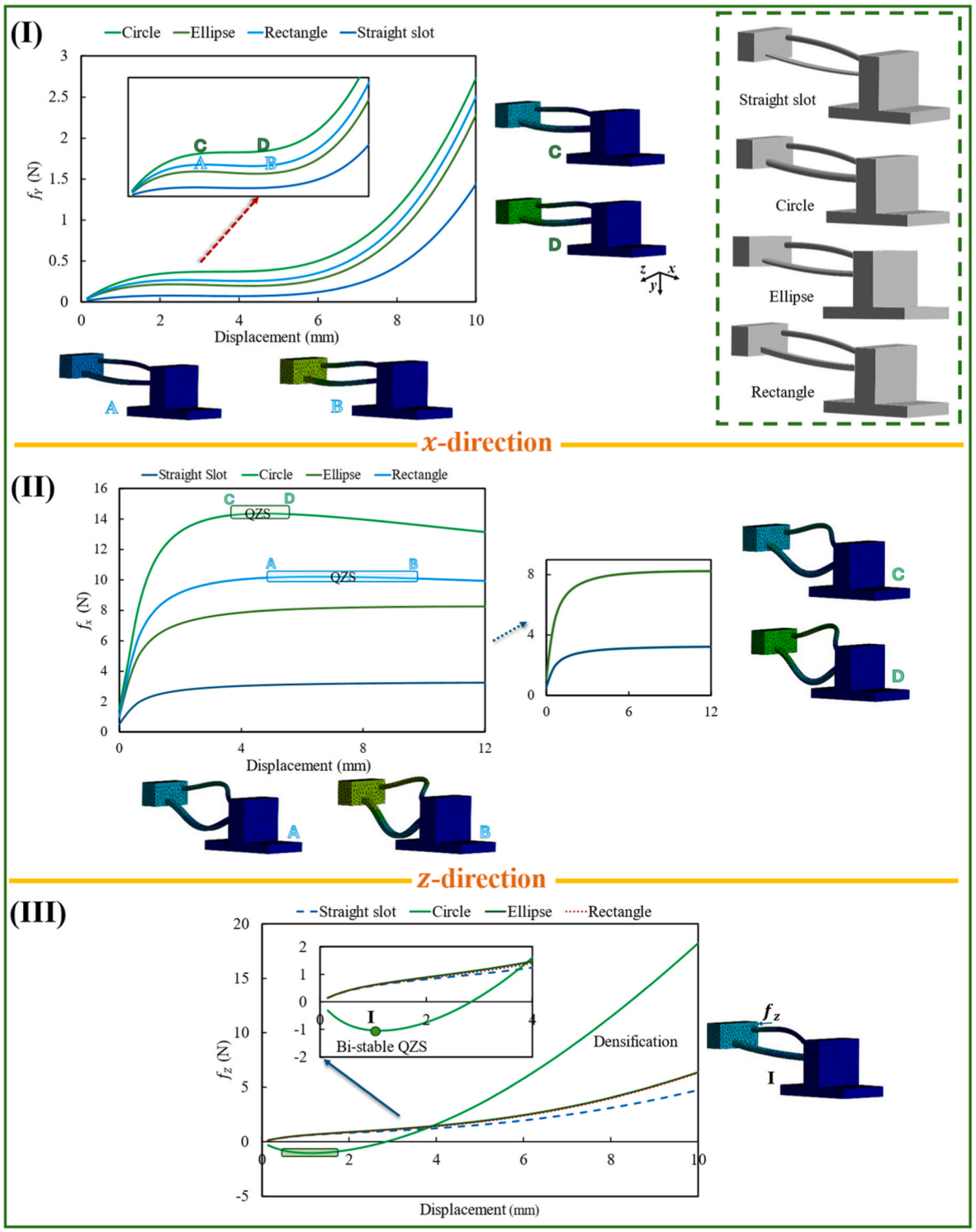


Fig. 16. Structural shape investigation and force-displacement analysis of Model II. **(I)** various geometric configurations of the supportive curve in Model II, along with corresponding force-displacement responses in the *y*-direction. **(II)** comparison of constant force levels and QZS characteristics in the *x*-direction for different strut shapes. **(III)** bi-stability and QZS behaviour in the *z*-direction for different strut shapes, highlighting the influence of geometry on the force response.

function of displacement δ, and δ_{max} is the maximum displacement during loading. If unloading occurs, some energy may be recovered elastically, represented by the area under the unloading curve:

$$ER = \int_{\delta_{max}}^{0} F_{unload}(\delta) d\delta \tag{4}$$

The dissipated energy is the portion of the absorbed energy that is not recovered upon unloading. It is the area enclosed by the hysteresis loop:

$$ED = EA - ER = \oint F(\delta)\, d\delta \tag{5}$$

Or, in case of full load-unload cycle:

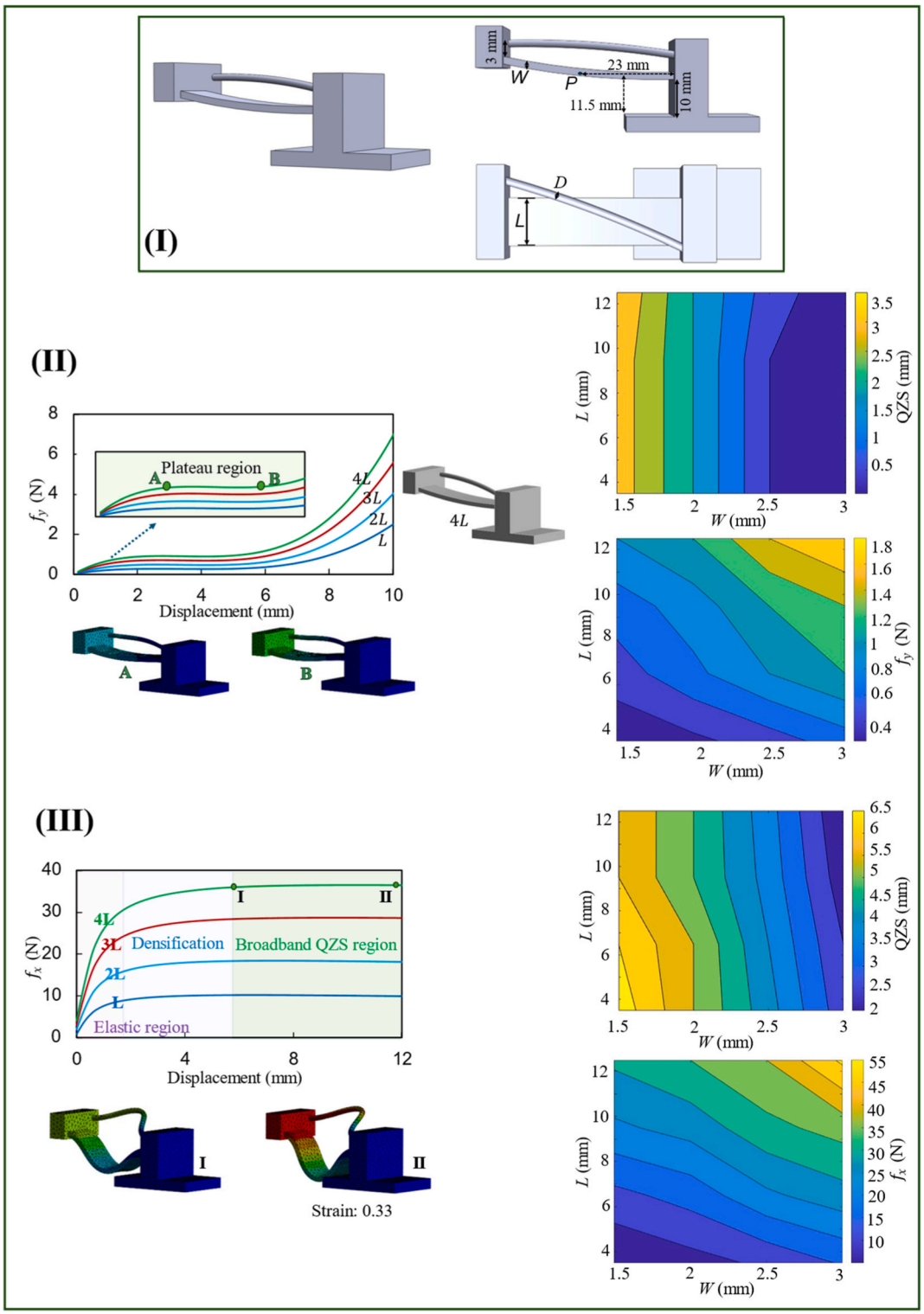


Fig. 17. Optimal configuration and parametric analysis of Model II. **(I)** selected layout of Model II with a rectangular supportive curve. **(II)** and **(III)** show the influence of *L* and *W* of the supportive curve on QZS characteristics and force response in the *y*- and *x*-direction, respectively.

$$ED = \int_0^{\delta_{max}} F_{load}(\delta)d\delta - \int_{\delta_{max}}^0 F_{unload}(\delta)d\delta \tag{6}$$

Finally, the dissipated energy can be calculated using trapezoidal rule on the force-displacement data.

Fig. 18(a) shows the FEM and experimental cyclic force-displacement response of Model I in the *x*-direction using 2.5 %EGS-reinforced TPU/PHA. The meta-stabiliser exhibits a broad plateau region approximately 6 mm in length with a constant force of 24.5 N. An energy dissipation of 80.59 N mm was recorded, which attributed to hysteresis effects. Fig. 18(b) illustrates the QZS properties along the *y*-direction, demonstrating a 3.2 mm plateau length with a constant force of 0.73 N and an energy dissipation of 4.15 N mm. Comparison between experimental and FEM results determines excellent agreement, with an average deviation of less than 3 %. Fig. 18(c) presents the QZS response

along the *z*-direction, where a wide hysteresis loop is observed, resulting in 35.2 N mm of energy dissipation. This behaviour is attributed to a stiffness-switching mechanism that occurred at 3.75 mm displacement, where the stiffness transitions from positive to negative, disrupting the energy flow and contributing to QZS functionality. Fig. 18(d) displays the response of Model I along the *x*-direction using the unreinforced TPU/PHA material. A constant force of 19.6 *N* is observed, with a QZS region length of 6 mm. By comparing Fig. 18(a) and (d), it is evident that 2.5 % EGS reinforcement improves energy dissipation by approximately 50 % and increases the constant-force level by 25 %, all while preserving the fundamental QZS characteristics. These findings confirm that EGS reinforcement not only enhances energy dissipation but also increases the tuneability of force levels in QZS metamaterials. Consequently, further optimisation can be approached from both material composition and geometric design perspectives.

Similarly, Fig. 19(a) illustrates the QZS behaviour of Model II in the *x*-direction, showing an extended plateau region of 7 mm and a constant force of 36 N. The corresponding energy dissipation was 162.13 N mm, which is approximately double that of Model I. Fig. 19(b) and (c) compare the force-displacement responses of Model II with and without 2.5 % EGS reinforcement. The reinforced model exhibited a 28 % increase in force level and a 50 % increase in energy dissipation while maintaining QZS properties. These results highlight the effectiveness of EGS reinforcement in enhancing the mechanical performance of QZS metamaterials.

Cyclic loading tests were repeated five times for each sample, and all cycles overlapped, indicating the absence of Mullins effect. This consistency confirms that the mechanical behaviour of the proposed metamaterials remains stable under repeated loading and unloading conditions. The maximum strain observed was 0.37, that is well within the plateau region of the hyper-elastic material. Additional loading-unloading studies (Fig. 11(V)) witnessed no residual strain for strains below 0.5, further supporting the material's elastic recovery capabilities. Overall, this study confirms that all developed QZS metamaterials exhibit full strain recovery due to their visco-hyper-elastic properties. As a result, the 3D-printed meta-stabilisers demonstrate excellent mechanical resilience and are suitable for practical applications, where repeated usage is expected without degradation in performance.

Additionally, the vibration modes of the developed Model I and Model II meta-stabilisers were analysed under various loading directions, using 2.5 % EGS-reinforced bio-composite. Figs. 20(I) and (II), and 20(III) present the experimental and FEM mode shapes of Model I corresponding to the *x*-, *y*-, and *z*-directions, respectively. Similarly, Figs. 21(I) and 21(II) illustrate the experimental and FEM deformation modes of Model II in the *x* and *y*-directions, respectively. In the FEM visualisations, regions with redder coloration indicate higher deformation and stress concentrations, highlighting zones of critical mechanical response. A comparison between the experimental and FEM-derived mode shapes shows a strong level of agreement. This analysis provides valuable insight into the deformation behaviour of the structures under directional displacement and further confirms the consistency between simulation results and experimental data.

6.4. *Mechanical behaviour of supercells*

Metamaterial configurations, referred to as *supercells*, can be engineered by systematically arranging multiple designed unit cells in series, parallel, or hybrid connections [56]. In this study, supercells were constructed by assembling two- and four-unit cells of Models I and II, arranged either horizontally/vertically or in hybrid configurations, as illustrated in Fig. 22. Further, a matrix-based formulation was developed to guide this systematic arrangement of tailored metamaterial architectures along the *x*- and *y*-directions.

Fig. 22(a) presents the force-displacement responses along the *x*-direction for a single unit cell, a two-unit supercell, and a four-unit supercell of Model I. The results show that the constant-force level increases by factors of 1.94 (94 % improvement) and 3.77 (277 % improvement) for the two- and four-unit supercells, respectively, compared to the single unit cell. Fig. 22(b) displays the force-displacement responses along the *y*-direction for Model I. Here, the two-unit and four-unit supercells exhibit force levels of 1.45 N and 2.75 N, corresponding to increases of 98 % and 276 %, respectively. Fig. 22(c)

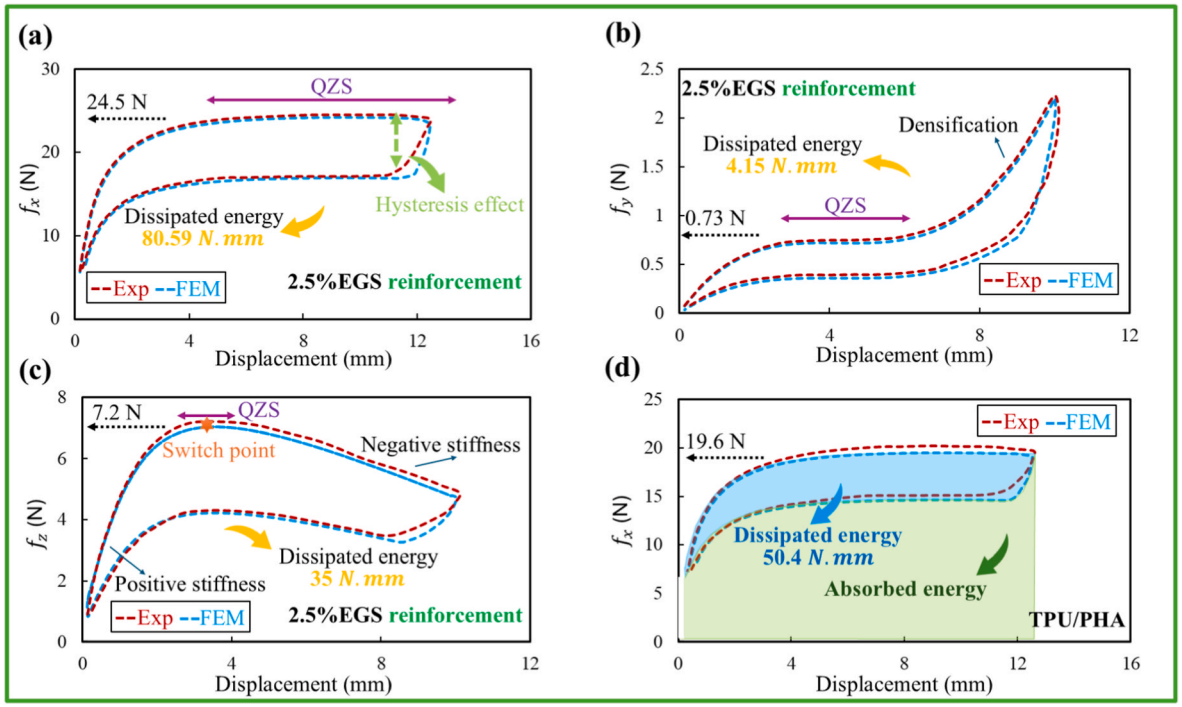


Fig. 18. Cyclic force-displacement performance of the Model I meta-stabiliser along different directions: **(a)** QZS response along the *x*-direction. **(b)** QZS response along the *y*-direction. **(c)** QZS response along the *z*-direction. **(d)** QZS response along the *x*-direction using unreinforced TPU/PHA.

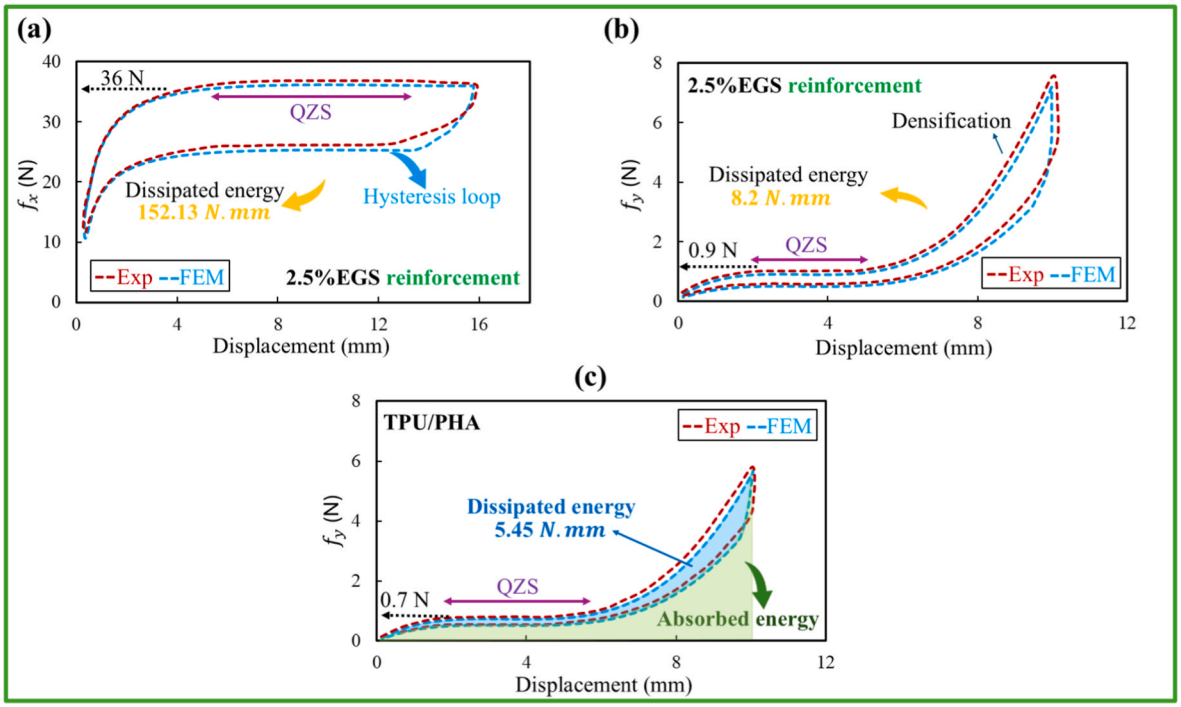


Fig. 19. Cyclic force-displacement performance of the Model II meta-stabiliser along different directions: **(a)** QZS response along the *x*-direction. **(b)** QZS response along the *y*-direction. **(c)** QZS response along the *y*-direction using unreinforced TPU/PHA.

illustrates the QZS behaviour of different configurations of Model I along the *z*-direction. Notably, the onset of the QZS plateau shifts from 3 mm in the single unit cell to 5.5 mm and 7 mm in the two- and four-unit supercells, respectively. In addition to the shift in the plateau onset, the constant-force level increases substantially with the inclusion of additional unit cells. Fig. 22(d) compares the force-displacement responses along the *x*-direction for Model II supercells with that of a single unit cell. The four-unit supercell achieved a constant-force level of 220 N, representing a 511 % increase, while the two-unit supercell reached 120 N, corresponding to a 233 % improvement. These findings confirm that both force (stress) and strain levels in the metamaterial structures can be effectively tuned and programmed over a wide range of configurations. From a practical perspective, the constant-force level can be adjusted between approximately 1 N and 220 N, depending on the application's specific requirements, while maintaining the characteristic QZS behaviour. Fig. 22(e) further highlights the tuneability of the QZS response across different configurations in the *y*-direction for Model II. The four-unit supercell achieved a constant-force level of 5.6 N (522 % improvement), while the two-unit supercell reached 2.9 N (222 % improvement) relative to the single unit cell. Also, the corresponding vibration mode shapes of the supercells are provided in Fig. 22(f).

In summary, this study demonstrates that by horizontally arranging multiple QZS meta-stabiliser unit cells, it is possible to design and fabricate advanced metamaterials with highly customisable and programmable mechanical responses.

6.5. *Vibration isolation performance of the developed meta-stabilisers*

This section experimentally evaluates the vibration isolation characteristics of the developed meta-stabilisers. The stiffness of the proposed metamaterials is intrinsically nonlinear, arising from both geometric and material contributions. This inherent nonlinearity necessitates precise preload control in practical applications to maximise vibration isolation efficiency. The results indicate substantial vibration attenuation over a wide frequency range at the optimal preload. However, the attenuation performance is influenced by both the excitation frequency and the acceleration magnitude. Accordingly, a comprehensive parametric analysis was conducted under varying excitation frequencies and acceleration amplitudes.

Fig. 23 presents the vibration attenuation performance of Model II under vertical loading at acceleration amplitudes of $g = 1$, 5, and 10 m/s^2. The QZS meta-stabiliser achieved up to 100 % vibration reduction under certain conditions. However, a slight decrease in attenuation efficiency was observed at higher excitation levels, attributed to increased system instability. Notably, the meta-stabiliser reduced the output vibration to 0.02 m/s^2 with an input periodic excitation of 0.22 m/s^2 at 50 Hz. Even under a high input excitation of 6.2 m/s^2, vibrations were attenuated to 0.71 m/s^2, corresponding to a 90 % reduction due to its QZS properties. The transient vibration response of the bio-composite meta-stabilisers (Models I and II) was further examined at the optimal preload for periodic excitations at 50, 100, and 150 Hz, with an input amplitude of 5 m/s^2. As shown in Fig. 23, Model II maintained high vibration mitigation performance across the frequency range, achieving an average reduction of approximately 92 % due to its nonlinear characteristics. Significant attenuation was also observed at lower excitation frequencies when the target preload was applied. Fig. 23(f) shows that Model II achieved an average vibration reduction of 83 %, decreasing excited signals from 3.6 to 0.6 m/s^2 at 50 Hz along the *x*-direction.

In addition, the vibration isolation performance of Model I was assessed in three orthogonal directions. At 50 Hz, it achieved an 88 % reduction in the *y*-direction (Fig. 24(a)), while reductions of 75 % and 77 % were recorded in the *x*- and *z*-directions, respectively (Fig. 24(b) and (c)). These results confirm that Model I exhibits effective multi-directional attenuation, enabled by its 3D-QZS properties.

To investigate the influence of material composition on isolation performance, both models were fabricated using unreinforced TPU/PHA and 2.5 wt% EGS-reinforced TPU/PHA bio-composites. Fig. 23(g) and (h) show that the reinforced material improved attenuation by approximately 30 % along the *y*-direction at 50 Hz and 100 Hz. For instance, at 100 Hz, the unreinforced meta-stabiliser reduced vibrations from 2.93 to 0.19 m/s^2, whereas the reinforced version achieved 0.13 m/s^2. These results, averaged over five tests, confirm the statistical robustness of the

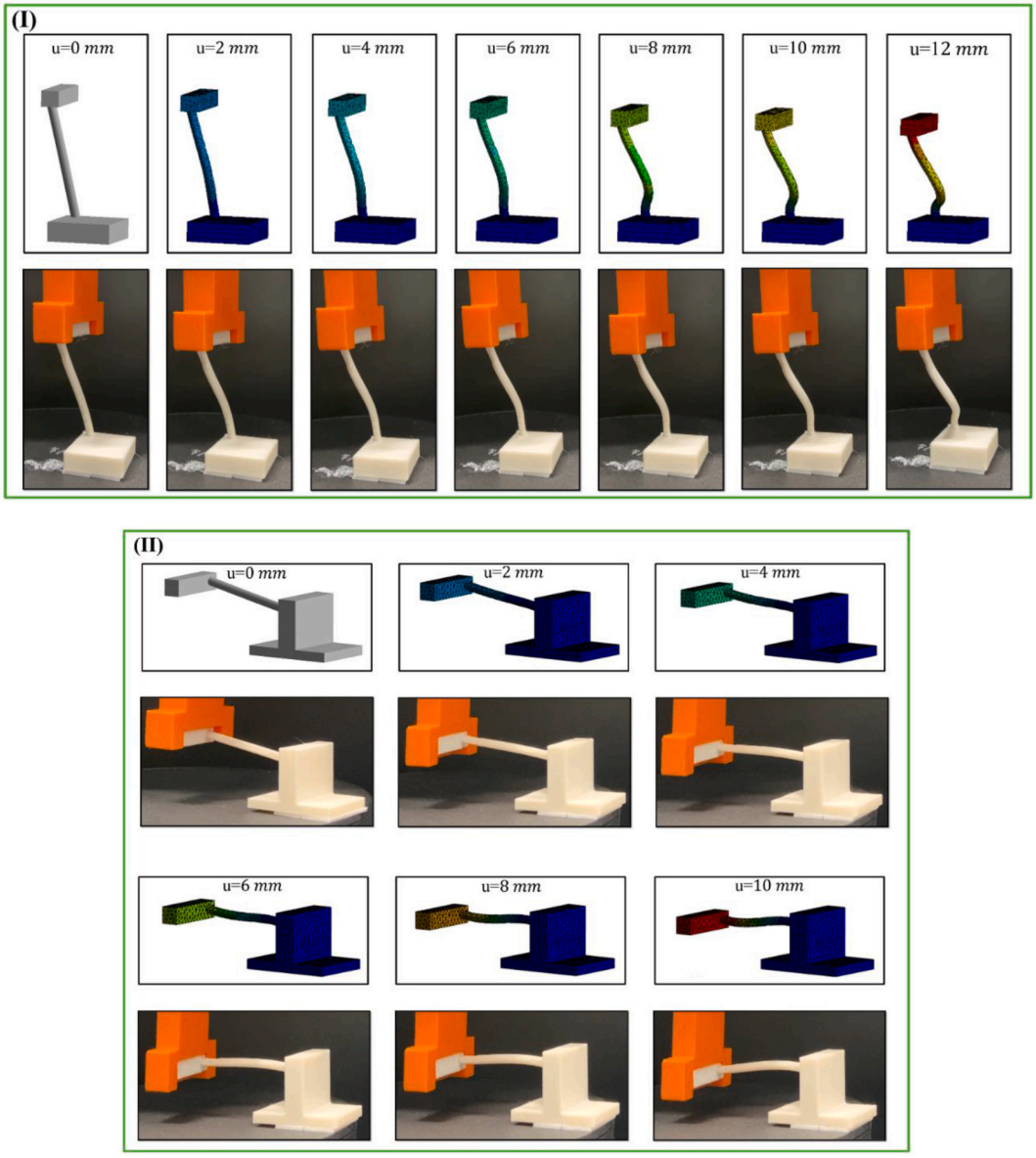


Fig. 20. Deformed mode shapes of Model I under different loading directions. **(I-III)** corresponds to the force-displacement study along *x*-, *y*-, and *z*-direction, respectively.

findings. Similarly, Fig. 23(i) demonstrates a 30 % improvement in the *x*-direction with EGS reinforcement. Furthermore, the vibration isolation performance of Model II at a low frequency of 10 Hz was evaluated using an incident excitation of 5 m/s^2, as shown in Fig. 23(j). The meta-stabiliser with 2.5 wt% EGS-reinforced TPU/PHA bio-composites achieved a 56 % reduction in vibration along the *y*-direction at 10 Hz. Compared to the 50–150 Hz range, vibration attenuation below 10 Hz remains challenging, as supported by previous studies [34–45].

To verify that this enhancement is independent of geometry, Model I was tested with both material compositions in all three directions (Fig. 24(a)–24(c)), again revealing an average improvement of approximately 30 %. This indicates that the observed vibration isolation improvements are attributable to the nonlinear visco-hyper-elastic properties of the reinforced bio-composite rather than geometric effects. Across both designs, the addition of 2.5 wt% EGS consistently improved vibration attenuation by approximately 30 % at various frequencies. Additionally, the supplementary material includes two videos (referred to as **Video 1** and **Video 2**), which correspond to the vibration tests performed on the developed meta-stabiliser Model II under acceleration conditions of $g = 5$ and 10 m/s^2, respectively. These recordings empirically demonstrate the model's practical efficacy in mitigating vibration amplitudes.

It is worth to note that the maximum operational strain of the meta-models lies within the range of 0.2–0.4 (as detailed in Section 6.2), corresponding to the strain range in which a pronounced plateau region forms in the reinforced TPU/PHA composite (Fig. 11(i)). Consequently, both material and geometric factors contribute to plateau formation within the operational strain range, enabling optimal vibration attenuation when the appropriate preload is applied.

The proposed meta-stabilisers demonstrate superior vibration isolation compared to existing QZS structures, achieving 100 % and 92 % reduction at g = 0.2 and 5 m/s^2, respectively, at 50 Hz. For example, Liu et al. [45] reported a vibration transmission loss of −8 dB at 50 Hz, while our meta-stabiliser achieved −20 dB at the same frequency. Zhao et al. [44] reported a 90 % vibration reduction between 100 and 600 Hz. Additionally, Liu et al. [36] achieved a 94.71 % reduction between 20

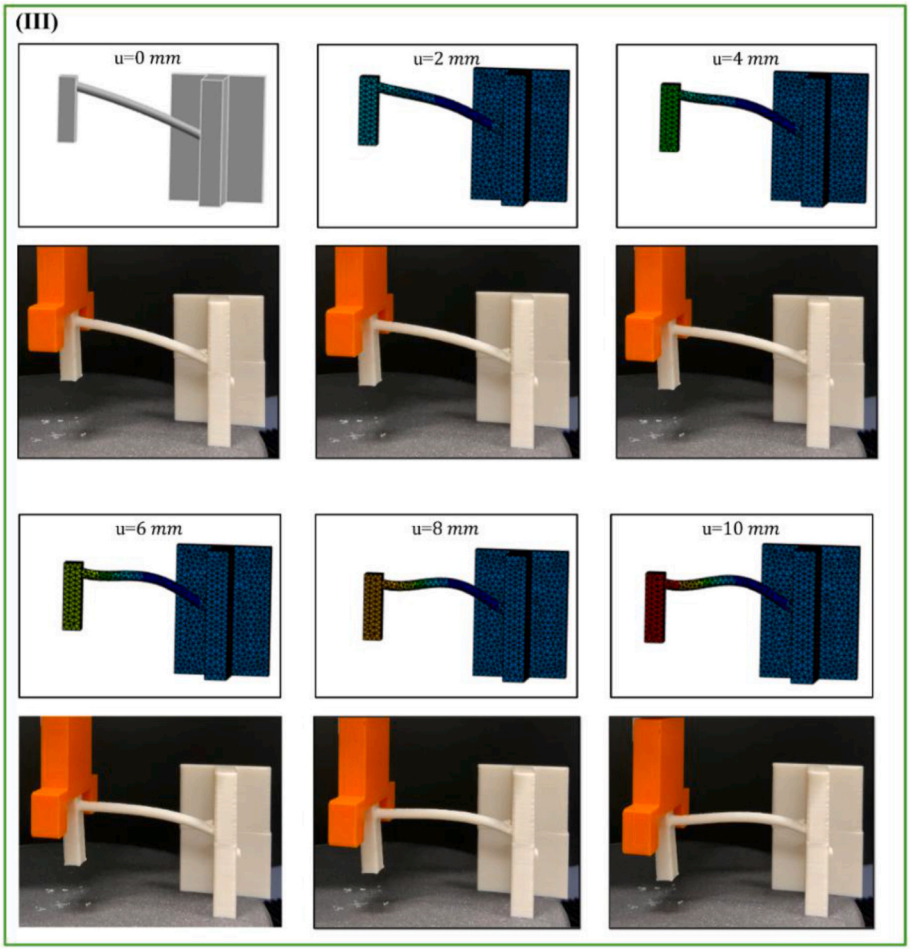


Fig. 20. (*continued*).

and 100 Hz using a single-layer QZS matrix structure with four unit cells.

7. Application prospects

The fabricated meta-stabilisers with the developed visco-hyper-elastic bio-composite, may present multiple promising applications across the automotive, aerospace, and biomedical engineering sectors. Focusing on the automotive domain, the proposed QZS meta-stabilisers can be implemented as intelligent damping elements within vehicle suspension systems, seat mounts, sensory and imaging housings. Of particular significance is their potential use as stabilising supports for health monitoring devices (HMDs), such as sensors and monitoring cameras, that are rigidly attached to a vehicle's chassis/body. By attenuating vibrations transmitted to these devices, the meta-stabilisers can improve measurement accuracy and device reliability. This is particularly important under dynamic driving conditions. As an example, Fig. 25 depicts the integration of the designed Model II meta-stabiliser into an autonomous vehicle platform (AURRIGO autonomous passenger transporter). In such platforms, multiple sensors are mounted both internally and externally to facilitate autonomous navigation and environmental perception. This meta-integration helps isolate sensors and cameras from road-induced vibrations, enhancing the performance and longevity of these key components.

Another practical demonstration involved the use of Model II as a stabiliser for a high-resolution camera mounted on an RC vehicle for off-road driving. The meta-stabiliser was mounted to the roof of the RC car, supporting a 4K wireless camera with an overall payload (camera plus accelerometer) of 90 *gr*, corresponding to the optimal constant-force of Model II. A wireless accelerometer was installed on the car roof to measure the input vibration, while a second accelerometer on the camera captured the output response. Fig. 26(II) shows the experimental setup, in which the system was subjected to irregular off-road terrain. Experimental results demonstrates that the meta-stabiliser reduced camera vibration levels by approximately 77 % (Fig. 26(I)). The test was repeated five times, with the average values reported to ensure statistical robustness and minimise experimental deviation. Figs. 23 and 26 demonstrate that the proposed meta-stabiliser can practically attenuate both periodic and random vibration propagations. These findings confirm the practical applicability of the proposed multidirectional QZS meta-stabilisers for automotive noise/vibration/harshness (NVH) mitigation in different environments. Additionally, supplementary video files, labelled **Video 3** and **Video 4**, are provided to showcase the results of driving tests performed under two different configurations: (i) with the camera mounted on the meta-stabiliser (**Video 3**), and (ii) with the camera rigidly attached to the vehicle roof (**Video 4**). These recordings clearly prove the capability of the meta-stabiliser to enhance video capture quality by mitigating vibration-induced image distortion. In addition to their performance advantages, the meta-stabilisers exhibit economic and environmental benefits. The manufacturing cost of both the stabiliser geometry and the reinforced bio-composite is relatively low compared to current active/passive control devices such as gyroscopes and electromechanical stabilisers, which require complex electronics, frequent calibration, and high maintenance costs. Moreover, the bio-composite comprises natural constituents, rendering the system more sustainable and environmentally responsible. Based on the current findings, the meta-stabiliser is expected to exhibit minimal residual strain under long-term cyclic loading. The maximum strain observed in the QZS region was 0.37, and additional loading-unloading experiments

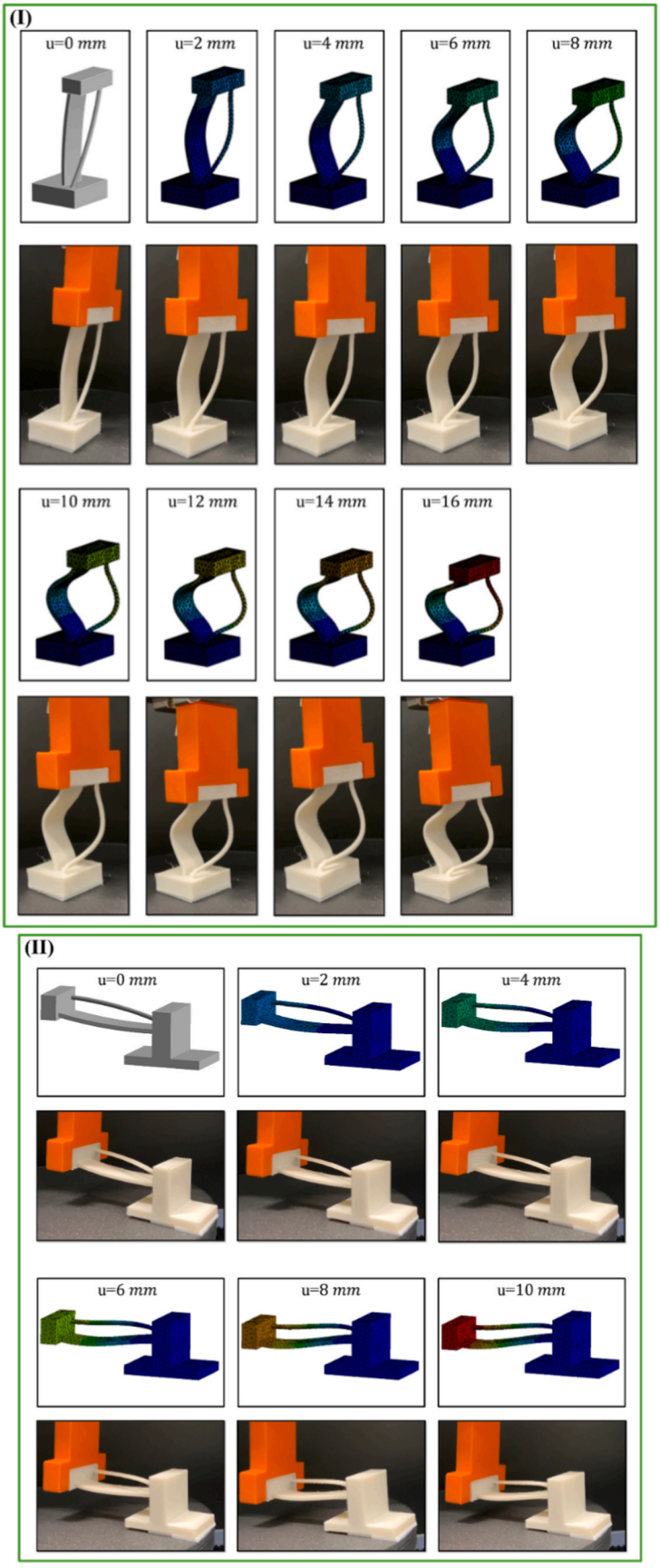


Fig. 21. Deformed mode shapes of Model II under different loading directions. **(I)** and **(II)** corresponds to the force-displacement study along *x*-, and *y*-direction, respectively.

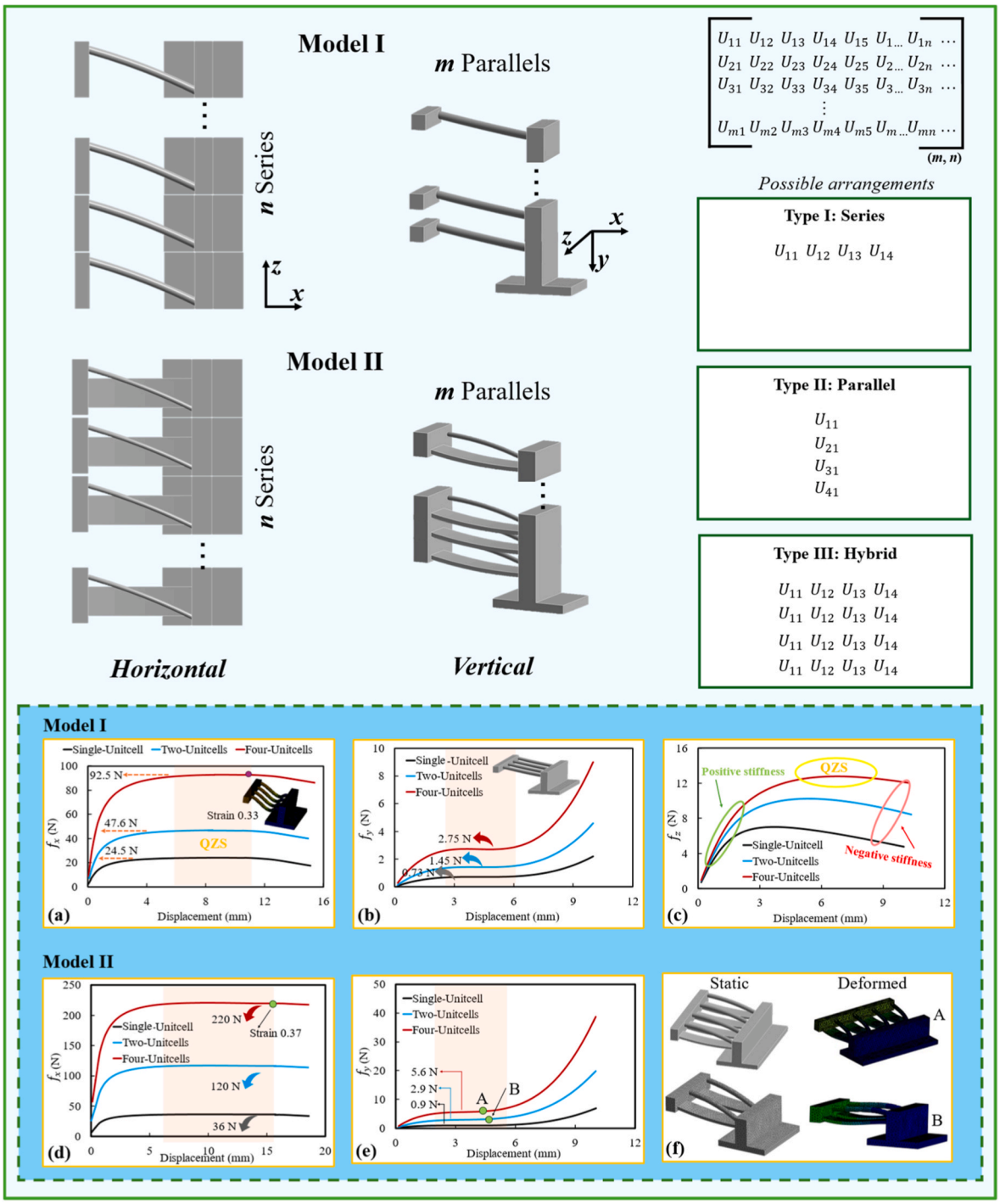


Fig. 22. Schematic assembly and force-displacement responses of programmable QZS metamaterials. **(a)–(c)** comparison of force-displacement responses for Model I in the *x*-, *y*-, and *z*-directions, respectively, between single-unit and supercell configurations. **(d)–(e)** comparison of force-displacement responses for Model II in the *x*- and *y*-directions, respectively, for single-unit and supercell configurations. **(f)** corresponding mode shapes associated with the *y*-directional response of Model II supercells.

(Fig. 11(V)) showed no residual strain for applied strains below 0.5, further confirming the excellent elastic recovery of the material. For future work, a comprehensive study of long-term performance (fatigue) and sustained-load behaviour (creep) will be conducted on the 2.5 wt% EGS-reinforced TPU/PHA bio-composite to better understand its long-term mechanical performance. Additionally, it is anticipated that, similar to other hyper-elastic materials, the TPU/PHA matrix will exhibit a reduction in stiffness with increasing temperature, which could influence both its cyclic and creep responses [57].

In summary, the proposed meta-stabilisers with tuneable QZS behaviour and a sustainable bio-composite, offer a simple, cost-effective, energy-efficient, and environmentally friendly alternative to conventional vibration isolation and stabilisation systems. Their demonstrated effectiveness in automotive applications, particularly for stabilising HMDs and precision sensors, suggests strong potential for adoption in engineering platforms where weight, reliability, and NVH control are critical.

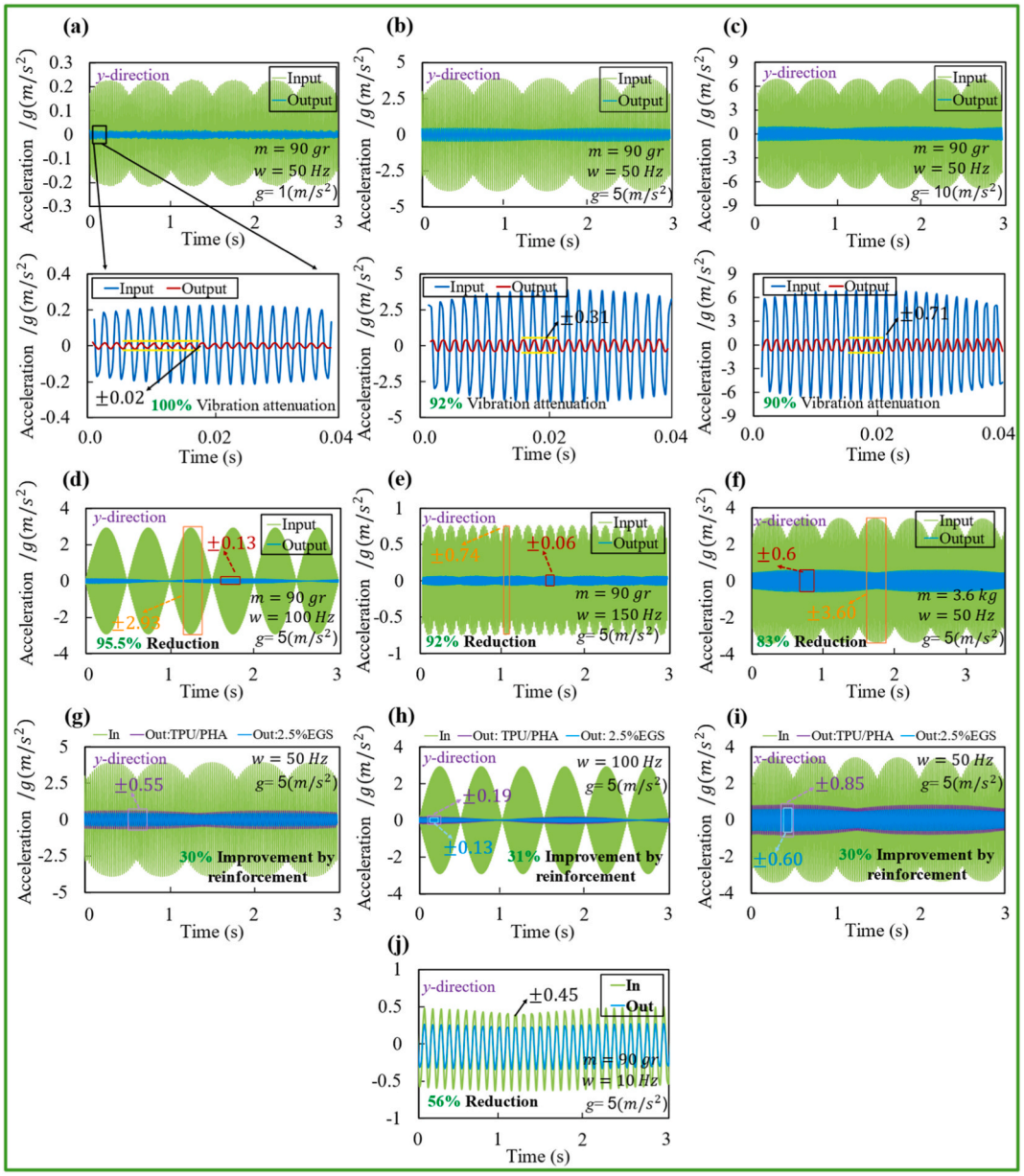


Fig. 23. Vibration testing results for Model II. **(a)–(c)** illustrate the vibration response along the *y*-axis at a frequency of 50 Hz under accelerations of $g = 1$, 5, and 10 m/s^2, respectively. **(d)** and **(e)** present the response along the *y*-axis at $g = 5$ m/s^2 for excitation frequencies of 100 Hz and 150 Hz, respectively. **(f)** shows the vibration behaviour along the *x*-axis at 50 Hz. **(g)** and **(h)** compare the vibration attenuation performance of Model II with and without 2.5 % EGS reinforcement along the *y*-axis at 50 Hz and 100 Hz, respectively. **(i)** provides a comparison of the vibration attenuation behaviour with and without 2.5 % EGS reinforcement along the *x*-axis at 50 Hz. **(j)** represents the vibration response along the *y*-axis at a frequency of 10 Hz under accelerations of $g = 5$ m/s^2.

8. Conclusion

This study introduces the first reported multidirectional QZS meta-stabilisers, which integrates woodpecker-inspired curvilinear architectures with the newly developed sustainable bio-composite. A hybrid design framework was established, combining the nonlinear material reinforcement and an AI-design approach. This innovative framework allows for precise customisation of the plateau region and constant-force output. The optimal reinforcement formulation identified is a composite made of 2.5 wt% EGS-reinforced TPU/PHA, which demonstrates a remarkable synergy of enhanced mechanical strength and superior energy dissipation capabilities.

In addition, for the first time the developed composite was shown to generate a broad and stable plateau region within the operational strain range (0.2–0.8). The coupling between geometric QZS behaviour and the nonlinear visco-hyper-elastic characteristics of the bio-composite enabled unprecedented vibration attenuation performance. Experimental and numerical analyses confirmed stable QZS response, repeatable hysteresis loops, and negligible Mullins effect over multiple load cycles. The vibration isolation capability of the meta-stabilisers was rigorously assessed under both periodic and random excitations, with practical validation in autonomous vehicle applications. Key conclusions are as follows.

- *Mechanical performance:* Reinforcing TPU/PHA with 2.5 wt% EGS increased tensile strength by 20 % and energy dissipation by 60 %. Outstandingly, it uniquely generates a broad plateau region (0.2–0.8 strain), a feature unprecedented in similar damping materials.

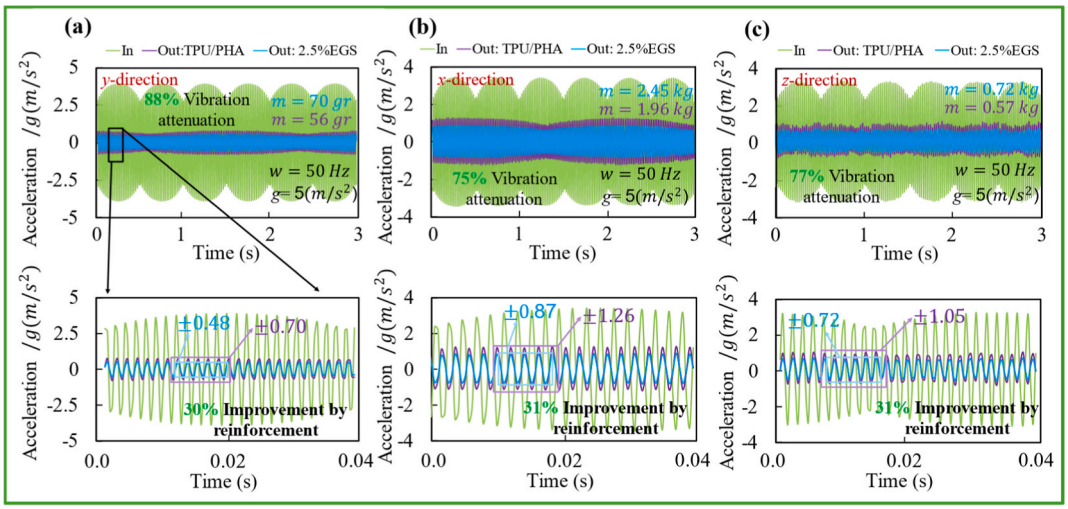


Fig. 24. Vibration testing results for Model I. **(a)–(c)** present the vibration response of Model I at a frequency of 50 Hz along the *y*-, *x*-, and *z*-axes, respectively. The magnified insets highlight the differences in signal output between configurations with and without 2.5 % EGS reinforcement under excitation in the corresponding directions.

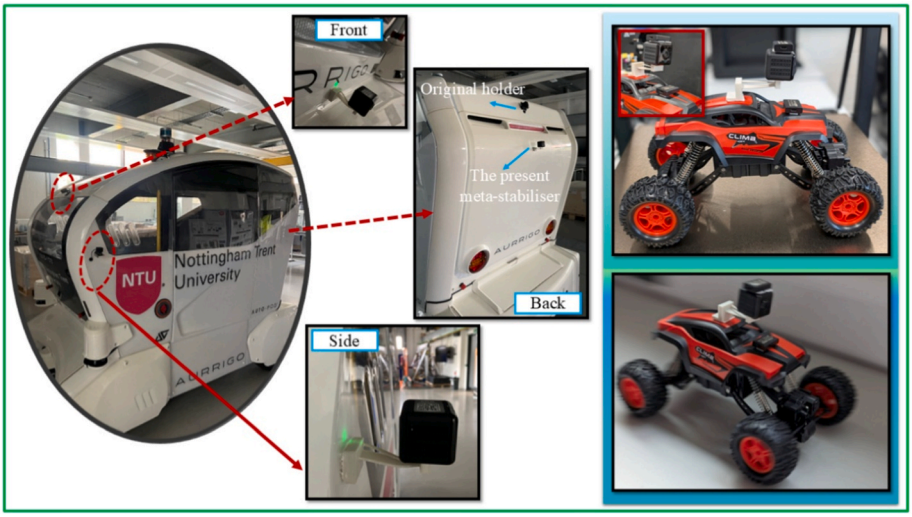


Fig. 25. Conceptual illustration of potential applications for the proposed QZS meta-stabilisers within the automotive industry, with particular emphasis on NVH control in autonomous and electric vehicles.

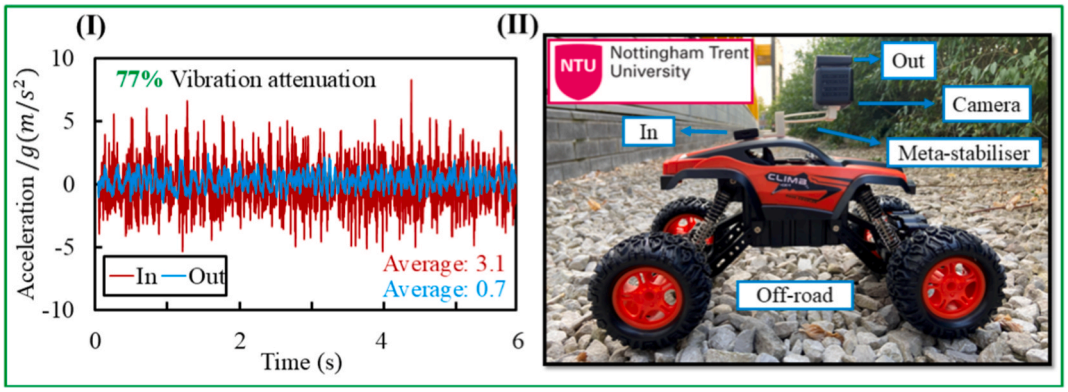


Fig. 26. Vibration testing of Model II mounted on an RC vehicle. **(I)** presents the results under random vibration excitation during off-road conditions. **(II)** illustrates the experimental test setup.

- *Bio-inspired design:* The meta-stabilisers were engineered by mimicking both the geometry and hyper-elastic material properties of the woodpecker's tongue-support mechanism.
- *Programmable QZS properties:* The QZS force level and operational range were structurally tuneable via design parameters, spanning 0.5–220 N in force and 1–7 mm in QZS displacement range, allowing application-specific customisation.
- *Vibration isolation:* Model II achieved up to 100 % suppression of periodic vibrations, while Model I achieved 88 % attenuation along three orthogonal axes. In random vibration testing, Model II reduced vibration by an average of 77 % during off-road RC vehicle tests.
- *Multi-directionality:* This work demonstrates, for the first time, the capability to achieve multidirectional QZS behaviour in a single structural system.
- *Scalability:* The modular supercell architecture allows tuning of constant-force levels and QZS displacement range through interconnected unit cell arrangements.
- *Cyclic durability:* Long-term operational stability was reported for the meta-stabilisers fabricated with the developed bio-composites. Five-cycle loading tests revealed no stiffness degradation and confirmed suppression of the Mullins effect.

In summary, the proposed meta-stabilisers combine bio-inspired design, sustainable materials, and programmable mechanics to deliver exceptional, multidirectional vibration isolation performance at a low manufacturing cost. Their proven effectiveness in autonomous vehicle and off-road applications, coupled with scalability and environmental sustainability, positions them as a transformative alternative to conventional active/passive NVH control systems in automotive, aerospace, and precision instrumentation sectors.

CRediT authorship contribution statement

Shawn Ravanbod: Writing – review & editing, Writing – original draft, Visualization, Validation, Software, Methodology, Investigation, Formal analysis, Data curation, Conceptualization. **Kaveh Rahmani:** Writing – review & editing, Writing – original draft, Methodology, Investigation, Data curation. **Callum Branfoot:** Writing – review & editing, Methodology, Investigation. **Sarah Karmel:** Writing – review & editing, Methodology, Investigation. **Abdul Haque:** Writing – review & editing, Methodology, Investigation. **Mark Lidgett:** Writing – review & editing, Methodology, Investigation. **Arash M. Shahidi:** Writing – review & editing, Supervision, Methodology, Investigation. **Andrew Alderson:** Writing – review & editing, Supervision, Methodology, Investigation. **Mahdi Bodaghi:** Writing – review & editing, Writing – original draft, Supervision, Resources, Project administration, Methodology, Investigation, Funding acquisition, Data curation, Conceptualization.

Declaration of competing interest

The authors declare that they have no known competing financial interests or personal relationships that could have appeared to influence the work reported in this paper.

Acknowledgement

The authors acknowledge the support by the Engineering and Physical Sciences Research Council (EPSRC) [I5M project, award number: EP/Y011457/1].

Appendix A. Supplementary data

Supplementary data to this article can be found online at https://doi.org/10.1016/j.mtadv.2025.100661.

Data availability

Data will be made available on request.

References

[1] M. Fleisch, A. Thalhamer, G. Meier, I. Raguż, P.F. Fuchs, G. Pinter, S. Schlögl, M. Berer, Functional mechanical metamaterial with independently tunable stiffness in the three spatial directions, Materials Today Advances 11 (2021) 100155, https://doi.org/10.1016/j.mtadv.2021.100155.
[2] K. Zhang, B. Yang, Z. Zhu, J. Fu, X. Han, W. Zhang, K. Dai, Structural optimized mechanical metamaterial for multi transient high-g impact suppression and self-monitoring, Mater. Des. 253 (2025) 113884, https://doi.org/10.1016/j.matdes.2025.113884.
[3] S. Yan, W. Liu, X. Tan, Z. Meng, W. Luo, H. Jin, Y. Wen, J. Sun, L. Wu, J. Zhou, Bio-inspired mechanical metamaterial with ultrahigh load-bearing capacity for energy dissipation, Mater. Today 77 (2024) 11–18, https://doi.org/10.1016/j.mattod.2024.06.003.
[4] G. Jiang, H. Zang, Y. Xiong, Y. Shen, Z. Guo, Y. Yang, M. Li, Design and vibration reduction performance analysis of a 6-DOF nonlinear vibration isolation platform by employing bio-inspired multi-joint X-structure, Nonlinear Dyn. 113 (16) (2025) 21119–21150, https://doi.org/10.1007/s11071-025-11256-3.
[5] T.A.M. Hewage, K.L. Alderson, A. Alderson, F. Scarpa, Double-negative mechanical metamaterials displaying simultaneous negative stiffness and negative poisson's ratio properties, Adv. Mater. 28 (46) (2016) 10323–10332, https://doi.org/10.1002/adma.201603959.
[6] C. Liu, J. Wang, W. Zhang, X.-D. Yang, X. Guo, T. Liu, X. Su, Synchronization of broadband energy harvesting and vibration mitigation via 1:2 internal resonance, Int. J. Mech. Sci. 301 (2025) 110503, https://doi.org/10.1016/j.ijmecsci.2025.110503.
[7] M. Bodaghi, A.R. Damanpack, W.H. Liao, Adaptive metamaterials by functionally graded 4D printing, Mater. Des. 135 (2017) 26–36, https://doi.org/10.1016/j.matdes.2017.08.069.
[8] H. Yang, N. D'Ambrosio, P. Liu, D. Pasini, L. Ma, Shape memory mechanical metamaterials, Mater. Today 66 (2023) 36–49, https://doi.org/10.1016/j.mattod.2023.04.003.
[9] R. Hamzehei, M. Bodaghi, N. Wu, Mastering the art of designing mechanical metamaterials with quasi-zero stiffness for passive vibration isolation: a review, Smart Mater. Struct. 33 (8) (2024) 083001, https://doi.org/10.1088/1361-665X/ad5bcc.
[10] X. Huang, X. Liu, J. Sun, Z. Zhang, H. Hua, Vibration isolation characteristics of a nonlinear isolator using euler buckled beam as negative stiffness corrector: a theoretical and experimental study, J. Sound Vib. 333 (4) (2014) 1132–1148, https://doi.org/10.1016/j.jsv.2013.10.026.
[11] K. Liang, Y. Jing, X. Zhang, Design of broad quasi-zero stiffness platform metamaterials for vibration isolation, Int. J. Mech. Sci. 281 (2024) 109691, https://doi.org/10.1016/j.ijmecsci.2024.109691.
[12] F. Zhao, J. Ji, K. Ye, Q. Luo, An innovative quasi-zero stiffness isolator with three pairs of oblique springs, Int. J. Mech. Sci. 192 (2021) 106093, https://doi.org/10.1016/j.ijmecsci.2020.106093.
[13] G. Wen, J. He, J. Liu, Y. Lin, Design, analysis and semi-active control of a quasi-zero stiffness vibration isolation system with six oblique springs, Nonlinear Dyn. 106 (1) (2021) 309–321, https://doi.org/10.1007/s11071-021-06835-z.
[14] X. Zhang, X. Lu, C. Li, R. Tian, L. Chen, M. Wang, Design of hyperbolic quasi-zero stiffness metastructures coupled with nonlinear stiffness for low-frequency vibration isolation, Eng. Struct. 312 (2024) 118262, https://doi.org/10.1016/j.engstruct.2024.118262.
[15] H. Fan, L. Yang, Y. Tian, Z. Wang, Design of metastructures with quasi-zero dynamic stiffness for vibration isolation, Compos. Struct. 243 (2020) 112244, https://doi.org/10.1016/j.compstruct.2020.112244.
[16] A. Carrella, M.J. Brennan, I. Kovacic, T.P. Waters, On the force transmissibility of a vibration isolator with quasi-zero-stiffness, J. Sound Vib. 322 (4–5) (2009) 707–717, https://doi.org/10.1016/j.jsv.2008.11.034.
[17] L. Li, F. Yang, S. Liu, Z. Guo, D. Han, Y. Xia, L. Wang, H. Fan, Design of quasi-zero-stiffness metamaterials with ultra-wideband vibration isolation performance, Int. J. Mech. Sci. 300 (2025) 110440, https://doi.org/10.1016/j.ijmecsci.2025.110440.
[18] Z. Zhang, Z. Qi, D. Pan, Design and test of a quasi-zero stiffness metastructure based on the preshaped beams for low-frequency vibration isolation, Mater. Des. 253 (2025) 113853, https://doi.org/10.1016/j.matdes.2025.113853.
[19] M. Mohammadi, A.Z. Kouzani, M. Bodaghi, A. Zolfagharian, 3D-printed programmable bistable mechanisms for customized wearable devices in tremor attenuation, J. Mech. Behav. Biomed. Mater. 168 (2025) 107006, https://doi.org/10.1016/j.jmbbm.2025.107006.
[20] J. Wang, G. Yao, Multi-directional vibration isolation performances of a scissor-like structure with nonlinear hybrid spring stiffness, Nonlinear Dyn. 112 (11) (2024) 8871–8888, https://doi.org/10.1007/s11071-024-09561-4.
[21] H. Hong, S. Kim, W. Kim, W. Kim, J. Jeong, S.S. Kim, Design optimization of 3D printed kirigami-inspired composite metamaterials for quasi-zero stiffness using deep reinforcement learning integrated with bayesian optimization, Compos. Struct. 359 (2025) 119031, https://doi.org/10.1016/j.compstruct.2025.119031.
[22] Y. Cai, Z. Wang, G. Liu, H. Qian, Y. Jiang, Dual-functional quasi-zero stiffness metamaterial for vibration isolation and impact attenuation, Int. J. Mech. Sci. 300 (2025) 110418, https://doi.org/10.1016/j.ijmecsci.2025.110418.

[23] P. Wu, S. Li, Z. Li, W. Xia, Y. Li, Modular QZS metamaterials with enhanced load adaptability for low-frequency vibration isolation, Smart Mater. Struct. 34 (5) (2025) 055017, https://doi.org/10.1088/1361-665X/add3dc.
[24] H. Zhou, J. Gao, Y. Chen, Z. Shen, H. Lv, P. Sareh, A quasi-zero-stiffness vibration isolator inspired by kresling origami, Structures 69 (2024) 107315, https://doi.org/10.1016/j.istruc.2024.107315.
[25] N. Yang, Y. Deng, Z.F. Mao, Y.T. Chen, N. Wu, X.D. Niu, New network architectures with tunable mechanical properties inspired by origami, Materials Today Advances 4 (2019) 100028, https://doi.org/10.1016/j.mtadv.2019.100028.
[26] K. Ye, J.C. Ji, An origami inspired quasi-zero stiffness vibration isolator using a novel truss-spring based stack Miura-ori structure, Mech. Syst. Signal Process. 165 (2022) 108383, https://doi.org/10.1016/j.ymssp.2021.108383.
[27] X. Liu, S. Chen, X. Tan, S. Li, B. Wang, A mechanical metamaterial with programmable arbitrary quasi-zero-stiffness regions, Compos. Appl. Sci. Manuf. 198 (2025) 109076, https://doi.org/10.1016/j.compositesa.2025.109076.
[28] X. Liu, S. Chen, B. Wang, X. Tan, A multi-dimensional quasi-zero-stiffness mechanical metamaterial with different directional vibration isolation capabilities, Smart Mater. Struct. 34 (4) (2025) 045013, https://doi.org/10.1088/1361-665X/adc4a4.
[29] G. Pan, X. Jiao, C. Lin, Z. Guan, J. Wu, H. Liu, H. Zhao, H. Huang, High load-bearing quasi-zero stiffness metamaterials for vibration isolation, Int. J. Mech. Sci. 293 (2025) 110225, https://doi.org/10.1016/j.ijmecsci.2025.110225.
[30] A.S. Dalaq, M.F. Daqaq, Experimentally-validated computational modeling and characterization of the quasi-static behavior of functional 3D-printed origami-inspired springs, Mater. Des. 216 (2022) 110541, https://doi.org/10.1016/j.matdes.2022.110541.
[31] S. Hou, J. Wei, A quasi-zero stiffness mechanism with monolithic flexible beams for low-frequency vibration isolation, Mech. Syst. Signal Process. 210 (2024) 111154, https://doi.org/10.1016/j.ymssp.2024.111154.
[32] H. Lu, L. Meng, W. Wang, J. Wang, Y. Wang, A study on an asymmetric quasi-zero stiffness metamaterial based on trigonometric function spatially rotated curved beams, Compos. Commun. 57 (2025) 102464, https://doi.org/10.1016/j.coco.2025.102464.
[33] R. Hamzehei, M. Bodaghi, N. Wu, Bio-inspired design and 4D printing of multi-stiffness wavy metamaterial energy absorbers/dissipators with shape recovery features, Eng. Struct. 327 (2025) 119538, https://doi.org/10.1016/j.engstruct.2024.119538.
[34] X. Zhou, H. Liu, J. Zhang, L. Ren, L. Zhang, Q. Liu, B. Li, C. Xu, L. Ren, 4D printed bio-inspired polygonal metamaterials with tunable mechanical properties, Thin-Walled Struct. 205 (2024) 112609, https://doi.org/10.1016/j.tws.2024.112609.
[35] G. Yan, H.-X. Zou, S. Wang, L.-C. Zhao, Z.-Y. Wu, W.-M. Zhang, Bio-inspired toe-like structure for low-frequency vibration isolation, Mech. Syst. Signal Process. 162 (2022) 108010, https://doi.org/10.1016/j.ymssp.2021.108010.
[36] C. Liu, X. Jing, X-mechanism guided topological design on quasi-zero stiffness meta-ring, Mech. Syst. Signal Process. 234 (2025) 112814, https://doi.org/10.1016/j.ymssp.2025.112814.
[37] B. Ding, X. Li, S.-C. Chen, Y. Li, Modular quasi-zero-stiffness isolator based on compliant constant-force mechanisms for low-frequency vibration isolation, J. Vib. Control 30 (3) (2024) 3006–3020, https://doi.org/10.1177/10775463231188160.
[38] X. Li, B. Ding, J. Ran, Ch Li, X. Dong, S.-C. Chen, Design and characterization of a compact tripod quasi-zero stiffness device for isolating low-frequency vibrations.", Precis. Eng. 91 (2024) 632–643, https://doi.org/10.1016/j.precisioneng.2024.10.013.
[39] Y. Chai, J. Bian, M. Li, A novel quasi-zero-stiffness isolation platform via tunable positive and negative stiffness compensation mechanism, Nonlinear Dyn. 112 (1) (2024) 101–123, https://doi.org/10.1007/s11071-023-09018-0.
[40] Q. Zhang, D. Guo, G. Hu, Tailored mechanical metamaterials with programmable quasi-zero-stiffness features for full-band vibration isolation, Adv. Funct. Mater. 31 (33) (2021), https://doi.org/10.1002/adfm.202101428.
[41] S. Ravanbod, K. Rahmani, S. Karmel, I. Pande, H. Amel, C. Branfoot, A.M. Shahidi, A. Alderson, M. Bodaghi, From coral to control: bio-inspired, 3D-printable metamaterials with tuneable quasi-zero stiffness and multi-functional bio-composites, Mater. Des. 257 (2025) 114398, https://doi.org/10.1016/j.matdes.2025.114398.
[42] W. Liu, S. Yan, Z. Meng, L. Wu, Y. Xu, J. Chen, J. Sun, J. Zhou, Programmable quasi-zero-stiffness metamaterials, Engineering (2024), https://doi.org/10.1016/j.eng.2023.11.027.
[43] C. Liu, R. Zhao, K. Yu, H.P. Lee, B. Liao, A quasi-zero-stiffness device capable of vibration isolation and energy harvesting using piezoelectric buckled beams, Energy 233 (2021) 121146, https://doi.org/10.1016/j.energy.2021.121146.
[44] J. Zhao, G. Zhou, D. Zhang, I. Kovacic, R. Zhu, H. Hu, Integrated design of a lightweight metastructure for broadband vibration isolation, Int. J. Mech. Sci. 244 (2023) 108069, https://doi.org/10.1016/j.ijmecsci.2022.108069.
[45] W. Liu, Q. Zhang, L. Wu, J. Sun, J. Zhou, Design of quasi-zero stiffness metamaterials with high reliability via metallic architected materials, Thin-Walled Struct. 198 (2024) 111686, https://doi.org/10.1016/j.tws.2024.111686.
[46] A.R. Damanpack, M. Bodaghi, W.H. Liao, A robust hyper-elastic beam model under bi-axial normal-shear loadings, Int. J. Non Lin. Mech. 95 (2017) 287–295, https://doi.org/10.1016/j.ijnonlinmec.2017.07.001.
[47] M. Bodaghi, A. Serjouei, A. Zolfagharian, M. Fotouhi, H. Rahman, D. Durand, Reversible energy absorbing meta-sandwiches by FDM 4D printing, Int. J. Mech. Sci. 173 (2020) 105451, https://doi.org/10.1016/j.ijmecsci.2020.105451.
[48] M. Lalegani Dezaki, R. Sales, A. Zolfagharian, H. Yazdani Nezhad, M. Bodaghi, Soft pneumatic actuators with integrated resistive sensors enabled by multi-material 3D printing, Int. J. Adv. Manuf. Technol. 128 (9–10) (2023) 4207–4221, https://doi.org/10.1007/s00170-023-12181-8.
[49] S. Rezaei, J. Kadkhodapour, R. Hamzehei, B. Taherkhani, A.P. Anaraki, S. Dariushi, Design and modeling of the 2D auxetic metamaterials with hyperelastic properties using topology optimization approach, Photon. Nanostruct: Fundam. Appl. 43 (2021) 100868, https://doi.org/10.1016/j.photonics.2020.100868.
[50] Z.D. Zhu, G.J. Ma, C.W. Wu, Z. Chen, Numerical study of the impact response of woodpecker's head, AIP Adv. 2 (4) (2012), https://doi.org/10.1063/1.4770305.
[51] J.-Y. Jung, S.E. Naleway, N.A. Yaraghi, S. Herrera, V.R. Sherman, E.A. Bushong, M. H. Ellisman, D. Kisailus, J. McKittrick, Structural analysis of the tongue and hyoid apparatus in a woodpecker, Acta Biomater. 37 (2016) 1–13, https://doi.org/10.1016/j.actbio.2016.03.030.
[52] P. Zhou, X.Q. Kong, C.W. Wu, Z. Chen, The novel mechanical property of tongue of a woodpecker, Journal of Bionic Engineering 6 (3) (2009) 214–218, https://doi.org/10.1016/S1672-6529(08)60126-2.
[53] L. Wang, S. Lu, X. Liu, X. Niu, C. Wang, Y. Ni, M. Zhao, C. Feng, M. Zhang, Y. Fan, Biomechanism of impact resistance in the woodpecker's head and its application, Sci. China Life Sci. 56 (8) (2013) 715–719, https://doi.org/10.1007/s11427-013-4523-z.
[54] P. Rosaiah, D. Yue, K. Dayanidhi, K. Ramachandran, P. Vadivel, N.S. Eusuff, V.R. M. Reddy, W.K. Kim, Eggshells & eggshell Membranes– A sustainable resource for energy storage and energy conversion applications: a critical review, Adv. Colloid Interface Sci. 327 (2024) 103144, https://doi.org/10.1016/j.cis.2024.103144.
[55] N.E. Putra, R. Youf, V. Moosabeiki, M.A. Leeflang, M. Klimopoulou, M.J. Mirzaali, A. Mol, M. Riool, L.E. Fratila-Apachitei, J. Zhou, I. Apachitei, A.A. Zadpoor, Direct ink writing of sustainable multifunctional biodegradable porous Fe-eggshell scaffolds, Acta Biomater. (2025), https://doi.org/10.1016/j.actbio.2025.06.051.
[56] J. Zhong, J. Li, B. Ding, S.-C. Chen, Design and experimental verification of programmable metastructures based on constant force cells, Smart Mater. Struct. 34 (1) (2025) 015002, https://doi.org/10.1088/1361-665X/ad95cd.
[57] X. Chen, A. Li, Y. Zhang, Temperature effect on thermal, mechanical, and electrical properties of Ag nanoparticle filled thermoplastic polyurethane composites, Polym. Compos. 42 (11) (2021) 5952–5961, https://doi.org/10.1002/pc.26276.